Investigating the Space Weather Impact of the 2003 Halloween Geomagnetic Storm by the Ground Magnetic Field Variations: a Global View

Hongyi Hu[1]

[1]The Overlake School

April 20, 2023

Abstract

Space weather is the phenomenon of solar storms and other events in space that can have impacts on Earth. They are a major concern for power grids which can be severely damaged by geomagnetic field variations during such natural phenomena. To reduce such impact and the possible consequences following, the study aims to determine how the storm's impact spreads across the Earth during a strong event, the October 29th, 2003 Halloween Storm. The impact of the Halloween Storm is analyzed by using global maps of geomagnetic variations to find where it is received and how it propagated. Cross-correlation is done on specific latitudinal and longitudinal distributed chains. The maps show that impacts are received first in high-latitude regions and then propagate toward mid- and low-latitude regions. The regions of impact during the first storm are on the magnetic dayside while the second storm is on the magnetic night side. The cross-correlation study shows that localized patterns occur more in the high-latitude regions with more intensive impacts, such as Norway, Finland, Sweden, Russia, and Canada. Global patterns occur more in the mid and equatorial regions with less intensive impacts. The mid-latitude countries such as France, UK, and the US can also be impacted during extreme events. The visualization package is developed and available to researchers and the industry. The global view of space weather impacts can help us to understand and mitigate the hazardous impacts on modern society.

Investigating the Space Weather Impact of the 2003 Halloween Geomagnetic Storm by the Ground Magnetic Field Variations: a Global View

Hongyi Hu[1]

[1]The Overlake School

Abstract

Space weather is the phenomenon of solar storms and other events in space that can have impacts on Earth. They are a major concern for power grids which can be severely damaged by geomagnetic field variations during such natural phenomena. To reduce such impact and the possible consequences following, the study aims to determine how the storm's impact spreads across the Earth during a strong event, the October 29th, 2003 Halloween Storm. The impact of the Halloween Storm is analyzed by using global maps of geomagnetic variations to find where it is received and how it propagated. Cross-correlation is done on specific latitudinal and longitudinal distributed chains. The maps show that impacts are received first in high-latitude regions and then propagate toward mid- and low-latitude regions. The regions of impact during the first storm are on the magnetic dayside while the second storm is on the magnetic night side. The cross-correlation study shows that localized patterns occur more in the high-latitude regions with more intensive impacts, such as Norway, Finland, Sweden, Russia, and Canada. Global patterns occur more in the mid and equatorial regions with less intensive impacts. The mid-latitude countries such as France, UK, and the US can also be impacted during extreme events. The visualization package is developed and available to researchers and the industry. The global view of space weather impacts can help us to understand and mitigate the hazardous impacts on modern society.

Plain Language Summary

Space weather is the phenomenon of solar storms and other events in space that can have impacts on Earth. They are a major concern for power grids which can be severely damaged during such natural phenomena. To reduce the impact and the possible consequences, the study aims to determine how the storm's impact spreads across the Earth during a strong event: the October 29th, 2003 Halloween Storm. The impact of this storm is analyzed using a global map of geomagnetic variations to find the progression. Cross-correlation is applied to distinguish the global and localized features of impacts. The maps show that impacts are received first in high-latitude regions and then propagate toward lower latitude regions. The cross-correlation study shows that localized patterns occur more in the high-latitude regions with more intensive impacts, such as Norway, Finland, Sweden, and Canada. Global patterns occur more in the mid and equatorial regions with less intensive impacts. The mid-latitude countries such as France, UK, US can also be impacted during extreme events. The visualization package is developed and available to researchers and the industry. The global view of space weather impacts can help us to understand and mitigate the hazardous impacts on modern society.

1 Introduction

Space weather is the phenomenon of solar storms and other events in space that can have an impact on Earth. The main source of space weather is the Sun, which can produce solar flares (Hood & Priest, 1979; Kusano et al., 2004, 2012; Shibata & Magara, 2011), coronal mass ejections (CMEs) (Mcallister et al., 1996; Forbes, 2000; Webb et al., 2000; Hathaway & Wilson, 2006), and high-speed solar wind streams that cause significant impacts on modern society (Eastwood et al., 2017), affecting technologies such as radio communication, GPS and GNSS systems, and satellite communications, high-latitude aviation, Mining operations, power grids, and natural gas pipelines (Baker et al., 2008; Berger et al., 2020) . The results can disrupt radio communications, endanger astronauts, cause errors in GPS and GNSS systems, lose satellite communications, expose pilots and passengers to higher levels of radiation in high-latitude aviation, overload power grids, and accelerate corrosion of natural gas pipelines (Osella et al., 1998). As a result, space weather has significant implications for national security due to the capability to damage critical infrastructures, such as the electric grid. The US has a large space-based infrastructure and is almost exclusively reliant on an aging and stressed power grid, making it vulnerable to the effects of space weather. To mitigate these effects, the US has established a Federal Operating Concept for Impending Space Weather Events (FEMA Homeland Security, 2019), which focuses on operational and crisis planning. Space weather study has become one of the most important research in recent years.

Geostorms result in anomalies and disruptions to modern conveniences such as electrical power distribution networks. Space weather conditions on the ground generally originate from the interaction of the solar wind with the magnetosphere, which propagates down to the ionosphere and ground via magnetic field lines (Shiokawa, 2023). Geomagnetically induced currents (GICs) are set up by a geoelectric field (E) which arises from time variations in magnetic field B caused by ionospheric and magnetospheric currents and the conductive properties of the ground. The GICs can cause severe damages of power grids. Extreme space weather events are now recognized as a serious threat to worldwide technological infrastructure, e.g., (Boteler et al., 1998; Viljanen, 1997; Pulkkinen et al., 2017). For example, during the 1989 storm (D. H. Boteler, 2019), the entire grid was out of service within 90 seconds. The collapsed power grid left six million people and the rest of Quebec without electricity for nine hours in most places, and days in others. This geomagnetic storm caused about $10 million dollars in damage to Quebec and tens of millions customers out of services. Extreme B field variations during the storm can be generated with a variety of spatial scales. They can occur in the auroral zone with fine spatial scales ($<\sim$100 km) or be excited by CMEs (Srivastava & Venkatakrishnan, 2002) and interplanetary shocks with global scales (Ngwira et al., 2013, 2015; Belakhovsky et al., 2018, 2019; Engebretson et al., 2019). Magnetometers have proven essential in this area for both research and real-time monitoring of B that drives GIC. Forecasting large GIC remains challenging as the largest GIC is not always concurrent with the largest geomagnetic depressions (Dimmock et al., 2019; Tóth et al., 2007) or elevated geomagnetic activity levels (Engebretson et al., 2020). So, it is important to use magnetometer observation to investigate the physics mechanism behind GICs and to verify the model predictions with observations (Kotzé et al., 2015). Since the 2003 Halloween Storm is the most intense storm in recent three decades, It has been studied by many researchers with different focus, such as the geomagnetic disturbance at lowest latitudes in the dayside hemisphere (Villante & Regi, 2008; Barbosa et al., 2015), the equatorial anomaly in the Brazilian sector(Batista et al., 2006), impacts on power grids at mid-latitudes(Schultz, 2012), geoelectric hazard maps for the Mid-Atlantic United States(Love et al., 2018), GICs on power network in New Zealand (Marshall et al., 2012), in Brazil (Barbosa et al., 2015), in Spain (Torta et al., 2014), in Great Britain (Orr et al., 2021), in Scotland (Simpson & Bahr, 2020), and in Japan(Ebihara et al., 2021). An insightful collection of research articles is listed in (Knipp, 2015) and a Geophysical Monograph on GICs and their impacts on power systems is published by (Gannon, 2019).

In this research paper, the impact of the Halloween Storm is analyzed by using global maps of geomagnetic variations to find where it is received and how it propagated. There are magnetic field data from 205 magnetometer observatories available for the 2003 Halloween Storm, which makes it possible to look at the global picture of the storm's impacts on magnetic field variations. The map is generated with Kriging interpolation and cross-correlation is done on specific latitudinal distribution chains and longitudinal distribution chains. The maps show that impacts are received first in high-latitude regions and then propagate toward mid- and low-latitude regions. Examining magnetic field variations caused by this great storm at a global scale allows for a better understanding of the questions: How did the 2003 Halloween storm impact the regions of the Earth from the point of view of magnetic field variations? What is the correlation between the magnitude of impact between the different latitude and longitude regions? How do different regions of the Earth are impacted differently? The answers to these questions will provide observational information during a solar storm to power grid operations and other crucial infrastructures (*National Space Weather Strategy and Action Plan*, 2019). It will help them to mitigate potential hazards caused by space weather. Also, by comparing the predicted value of geomagnetic field variations to global maps, space weather researchers will be able to assess the prediction's accuracy and how the model can be improved to achieve better and more accurate results.

In this research paper, the methodology and data used are presented in section 2; the results of global maps of magnetic field variations, and latitude and longitude difference of magnetic field variations during the storms are presented in section 3; discussion and a summary of these results are concluded in section 4.

2 Data and Methodology

For this research, the 2003 Halloween Storm was picked as it is the strongest solar storm in the last three decades that impacted the Earth since one in 1989. The Halloween storm lasted three days and had several waves of storms. Only the first two storms on October 29th, 2003 were selected due to the limited scale of research and data available on solar wind conditions. Storm-1 is defined as the period between 06-09 UT based on the level of Interplanetary Magnetic Field (IMF) based on observations from ACE Satellite and Sym-H index shown in Figure 1. Storm-2 is defined as 17-24UT.

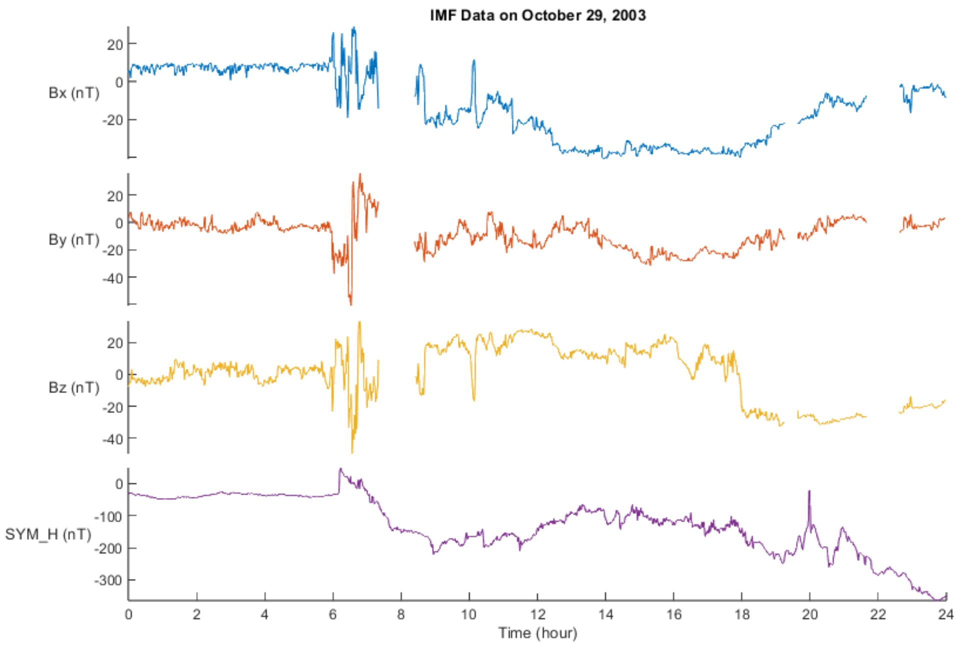

Figure 1: The missing data from the stacked plot is a result of extremely intense storms

There are two parts to the analysis. The first part was to develop global maps of magnetic variations during the Halloween Storm. The global map of magnetic field variations during the two storms was generated with MATLAB. The mesh grid was created with a precision of 1°. The base map loaded is the "landareas.shp" from the Mapping Toolbox™ in Matlab. The data points of the stations are then interpolated with Kriging interpolation (Xu et al., 2013) to generate a map, which is then overlaid on the base world map as "colormap" with the Matlab function mapshow(). The map is in the Projected Coordinate System so the geo coordinates match the Cartesian coordinates. Although the interpolation relies on Cartesian coordinates rather than geocoordinates, which means data points near the poles are skewed, this limitation is not significant enough for the purpose of this study. The accuracy of interpolation by kriging will also be limited as the number of stations is spatially sparse (Buck et al., 2002; Stoica & Moses, 2005).

After generating all the frames of global maps during the time interval, a Graphics Interchange Format (GIF) with all the frames was synthesized with PIL and glob modules in Python to easier observe the trend more over time. The frames and the GIF were used to predict the impact of the storm on modern society globally and its direction of spread by examining the geomagnetic impact on the map in chronological order. The second part is to perform a cross-correlation study between different regions on the Earth to find the different impacts between them.

Cross-correlation measures the similarity between two sets of time series data. It is used to determine how well two sets of data match up with each other by tracking the similarities (correlation coefficients) and the lag over time between each other. The possible range for the correlation coefficient is from 0 to +1.0. It can also determine the time lags between the sets of data.

The true cross-correlation sequence of two jointly stationary random processes, x_n and y_n, is given by

$$R_{xy}(m) = E\{x_{n+m}y_n^*\} = E\{x_n y_{n-m}^*\} \tag{1}$$

where $-\infty < n < \infty$, the $*$ denotes complex conjugation, and E is the expected value operator. The correlations with no normalization are

$$\hat{R}_{xy}(m) = \begin{cases} \sum_{n=0}^{N-m-1} x_{n+m}y_n^* & m >= 0 \\ \hat{R}_{xy}(-m) & m < 0 \end{cases} \tag{2}$$

and the output can then be normalized with

$$\hat{R}_{xy,coeff}(m) = \frac{1}{\sqrt{\hat{R}_{xx}(0)\hat{R}_{yy}(0)}}\hat{R}_{xy}(m) \tag{3}$$

To analyze how the longitude affects the two storms (Storm-1 and Storm-2), a few chains of stations are selected to run cross-correlation. In each chain, the stations are evenly distributed around the globe with varying magnetic local times (MLT) but a similar magnetic latitude. As the physics mechanisms behind this study are dependent on the magnetic field rather than geography, magnetic coordinates are used instead of geographical coordinates. The latitudes chosen are high-north, mid-north, equator, and south. Therefore a total of four chains for each storm is chosen. After stack plotting these stations with plot() function in Matlab, it was observed that the most significant feature of Storm-1 was between the period 05:59-07:39 UT on October 29th and that of Storm-2 between 17:24 21:34 UT. Any missing data in the series are linearly interpolated with R.

To analyze how the latitude affects the two storms, two chains for each storm were picked with varying latitudes and similar longitude. For Storm-1, one chain is before noon of MLT and the other is right after. The two chains of Storm-2 are before and after midnight of MLT. The stations chosen for Storm-1 is mostly identical to those for Storm-2 as the two storms are almost twelve hours apart. The difference between the two sets of stations chosen comes from the lack of available data for some of the stations in the other storm. For example, station AAE was chosen for the pr-midnight chain but not for the prenoon chain, and ELT was chosen for the prenoon chain but not for the pre-midnight chain.

For each chain, the series of data from the stations are cross-correlated with xcorr() function in Matlab and then stored the max correlation coefficients and the lags. Using this correlation and lag, two matrix colormaps for each chain were generated using pandas, seaborn and matplotlib modules in Python. A colormap is a matrix of values that define the colors for graphics objects such as surface, image, and patch objects. The colormap is drawn by mapping data values to colors in the colormap. By speculating the matrix colormaps, the local and global patterns of magnetic field variations at different stations can be revealed.

Data with a time resolution of one minute and a time interval from 00:00 UT, October 29, 2003 to 23:59 UT, October 29, 2003 was downloaded from SuperMAG (`supermag.jhuapl.edu`). Stations that contain more than 20 missing data points at the beginning or end of each of the two time periods (05:09 - 09:09 UTC, Oct. 29, 2003, and 17:24 UT, Oct. 29, 2003 - 00:24 UT, Oct. 30, 2003) were removed due to the inaccurate interpolation results of linear interpolation with an open end. That is when only one end of the period in interpolation was defined. This leaves 193 quality stations for the first period and 188 for the second. Solar wind data are from ACE satellites in the NASA database (https://sohoftp.nascom.nasa.gov/sdb/goes/ace/daily/). The temporal resolution of data is 60 seconds. The Interplanetary Magnetic Field (IMF) data are split into three components in Geocentric Solar Magnetospheric (GSM) coordinate (Maus & Lühr, 2005).

All datasets used in the study were open-source/publicly available. Data generated by this research project can be accessed at (`https://github.com/PythonOrC/SpaceWeather`)

3 Results

3.1 global maps of magnetic field variations

For the series of storms that happened during the three days of the 2003 Halloween Storm, the first two storms were selected for this research project. Storm-1 is defined as the period between 06-09 UT based on the level of satellite-based Interplanetary Magnetic Field (IMF) and ground-based magnetic field measurements. Storm-2 is defined as 17-24UT.

Most of the activities and variations in Storm-1 were on the dayside around noon (MLT). At 05:59 UT, the value of IMF Bz first turned negative, meaning that reconnection will happen soon. At 06:13 UT [as shown in Fig 2(a), the impact of the negative IMF Bz in 05:59 UT showed up on the dayside near Finland, Norway, and Sweden with a Bn of -1000 nT. The time lag between IMF Bz turning southward (negative) and the impact on the ground magnetic field is 14 minutes, which is shorter than the statistical value of 20-25 minutes (Akasofu, 2007) due to the strong and fast CME impacts. At 06:20 UT [as shown in Fig 2(b), the dBn value was low as -2000nT in high-latitude regions on both hemispheres of the Earth (near Finland and Norway in the northern hemisphere and near station B15 in the southern hemisphere). This shows an enhancement of the storm. Then, at 06:49 UT [as shown in Fig 2(c)], the region of impact enlarged from the two local regions to all high-latitude regions and expanded toward mid-latitude regions in both hemispheres (near Germany, Denmark, Poland, and the northern UK in the northern hemisphere and near the South Atlantic Ocean and B04 in the Southern Hemisphere). The strongest dBn is less than -2800nT and more than 1500nT and presents an oval shape. At 07:02 UT[as shown in Fig 2(d)], the region of impact expanded to France and north of Spain with an intensity of about -800 nT in the northern hemisphere, South Africa (-900 nT), and Australia (-500 nT) in the southern hemisphere. Finally, at 08:05 UT [as shown in Fig 2(e)], the regions recovered from the storm impact with minor negative dBn variations globally in mid and high latitudes.

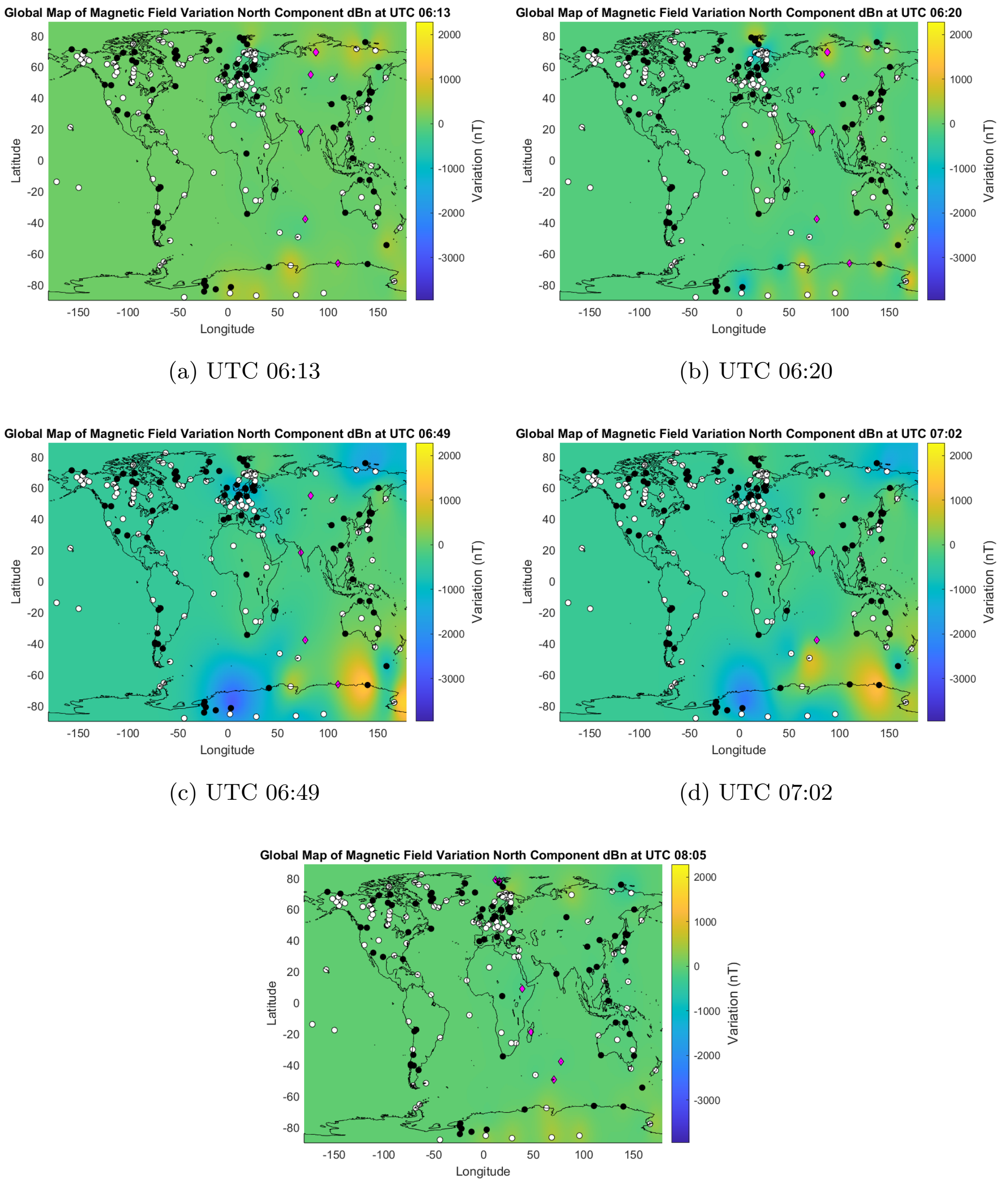

(a) UTC 06:13

(b) UTC 06:20

(c) UTC 06:49

(d) UTC 07:02

(e) UTC 08:05

Figure 2: Key frames in the progression of Storm 1. Yellow represents positive variation and blue represents negative variation, the black and white markers alternate every 10 degrees in terms of magnetic latitude. The purple markers represent the MLT noon.

For Storm-2, the main regions of impact are around Midnight MLT with several substorms happening one after another. The regions of impact were mostly near Finland, Norway, and Sweden. At 17:33 UT, a negative variation appeared on both sides of the pole with Svalbard reaching -700nT in the North and B04 Reaching -500nT in the South [as shown in Fig 3(a)]. Between 17:33 UT and 18:20 UT, there is a small substorm happening in both hemispheres with multiple positive-negative pairs observed. This indicates that there is a reconnection happening. At 18:20 UT, the storm started fading although IMF Bz is still

-20 nT[as shown in Fig 3(b)]. There are no significant changes even until 18:55 UT, which is when a new substorm happened [as shown in Fig 3(c)]. At 19:15 UT the variation intensity increased in Russia and Australia also rose in variation at 19:38 [as shown in Fig 3(d) and Fig 3(e)]. At 19:49 UT, this storm reached its peak impacts. Expanding to Danmark, the majority of Russia with max intensity of -2500 nT at KTN in the northern hemisphere, and south of New Zealand, South Indian Ocean, and South Pacific Ocean with the max impact of -2500 nT at MCQ in the southern hemisphere [as shown in Fig 3(f)]. The variations eased at 21:00 UT and another smaller substorm happened between 21:03 and 22:29 UT impacting Finland, Norway, and Sweden [as shown in Fig 3(g)].

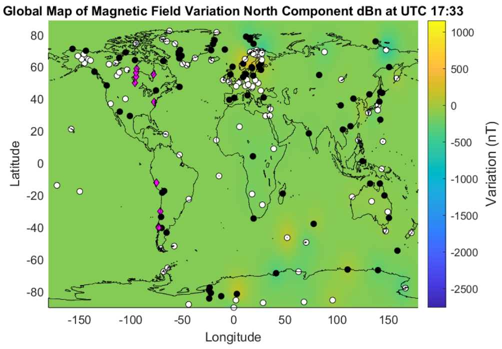

(a) UTC 17:33

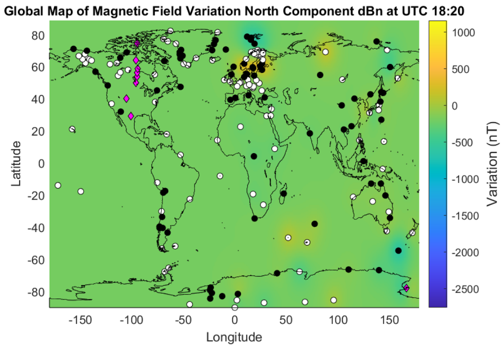

(b) UTC 18:20

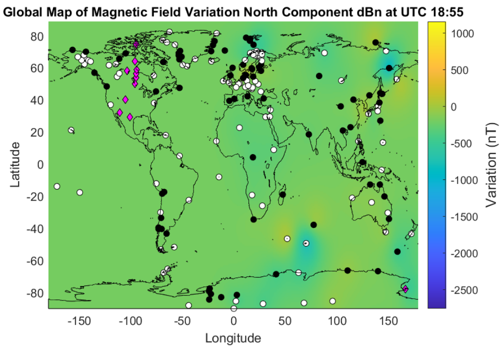

(c) UTC 18:55

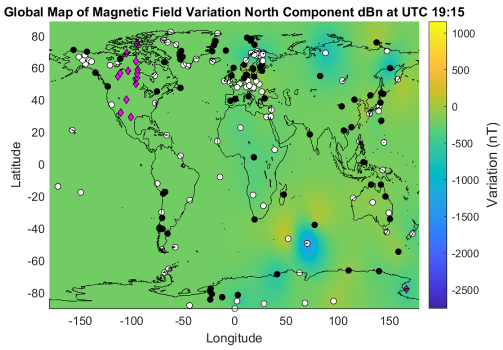

(d) UTC 19:15

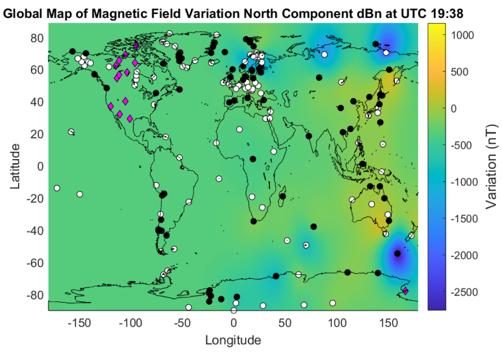

(e) UTC 19:38

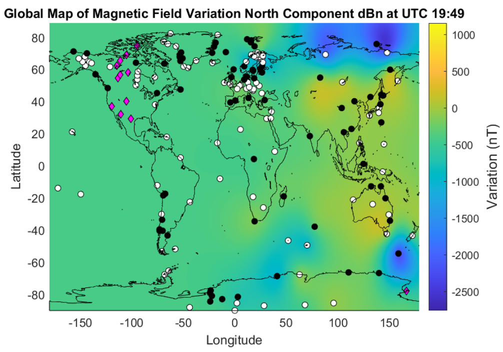

(f) UTC 19:49

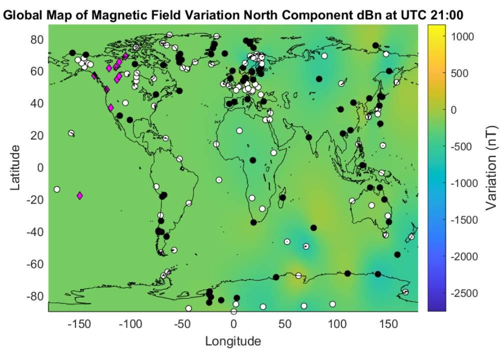

(g) UTC 21:00

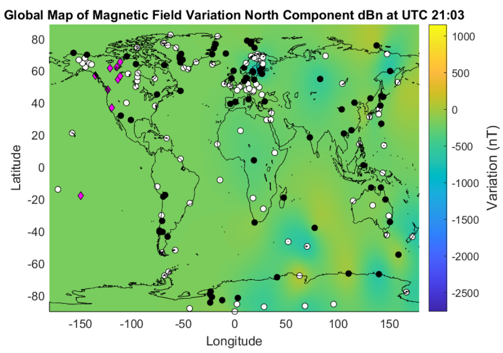

(h) UTC 21:03

Figure 3: Key frames in the progression of Storm 2. Same label setting as Fig 2

3.2 Cross-Correlation Study

By observing the colormaps of the cross-correlation for Storm-1 at pre-noon and afternoon MLT chains [as shown in Fig 4], it can be concluded that local signatures dominate high-latitude regions in both the northern and southern hemispheres shown by low correlation coefficients and large lags, such as ALE (MagLat 87.2°), HRN (MagLat 74.2°), BJN (MagLat 71.5°), MAW (MagLat -70.3°) in pre-noon chain and CHD (MagLat 65.1°), MGD (MagLat 53.9°), LEM(MagLat -53.2°), DRV (MagLat -80.5°) in afternoon chain. For mid- and low-latitude regions, from TAR (MagLat 54.5°) to CZT (MagLat -53.2°) in pre-noon chain and from MSR (MagLat 53.9°) to KDU (MagLat -21.8°) in the afternoon chain, the correlation coefficients between these stations are high and the lags between them are low, which indicates that there is a clear global signature between all of them. The maximum and minimum dBn value listed in Table 1 for prenoon chain and Table 2 for afternoon. It shows that the most intense variations occurring at 55°-70°MagLat regions for prenoon chain. For afternoon chain, only CHD and DRV shows strong disturbances of over 2000 nT while the rest of stations varying at a range of 200 nT. Overall, more local signatures dominate above 55°whereas the global signatures dominate stations below 55°.

IAGA	**MAGLON**	**MAG LAT**	**MLT**	**Min dBn**	**Max dBn**
MAW	90.3	−70.3	6.7	− 540.8	967.2
CZT	106.2	−53.2	7.8	− 814.6	2.9
LMM	100.1	−35.9	7.4	− 424.8	41.2
ELT	106.6	22.7	7.8	− 424.0	23.1
QSB	107.4	27.8	7.8	− 623.2	12.3
ISK	101.5	35.6	7.4	− 566.4	− 21.4
SUA	99.5	40.4	7.3	− 722.9	8.0
LVV	98.1	45.5	7.2	− 729.7	− 16.7
HLP	95.0	50.8	7.0	− 837.7	− 17.6
TAR	102.8	54.5	7.5	−1133.5	29.1
HAN	104.4	58.7	7.6	−1422.8	412.1
OUJ	106.0	61.0	7.7	−1598.1	914.3
SOD	107.1	64.0	7.8	−1771.3	617.3
SOR	105.9	67.4	7.7	−2082.6	399.1
BJN	107.8	71.5	7.9	−1342.8	595.1
HRN	109.0	74.2	7.9	− 506.4	675.4
ALE	94.0	87.2	6.9	− 263.3	2286.8

Table 1: Prenoon Chain Stations Info

IAGA	MAGLON	MAGLAT	MLT	Min dBn	Max dBn
DRV	−124.1	−80.5	16.4	− 103.1	1885.3
LEM	−133.2	−53.2	15.8	− 86.6	83.1
ASP	−152.7	−34.0	14.5	− 61.7	105.1
KDU	−155.2	−21.8	14.3	− 108.8	55.1
WEP	−145.3	−21.4	15.0	− 118.3	57.9
WEW	−144.3	−11.6	15.1	− 137.2	67.1
GUA	−144.0	6.2	15.1	− 137.7	62.5
CBI	−146.4	20.0	14.9	− 130.0	44.5
KAG	−157.2	24.8	14.2	− 124.6	58.8
HTY	−148.5	26.2	14.8	− 176.7	43.9
KAK	−148.0	29.3	14.8	− 149.4	31.9
ONW	−146.8	31.6	14.9	− 141.5	31.0
RIK	−144.7	36.7	15.0	− 137.9	42.8
MSR	−146.0	37.7	14.9	− 133.7	74.2
MGD	−140.4	53.9	15.3	− 121.6	117.5
CHD	−146.9	65.1	14.9	−1681.8	807.9

Table 2: Afternoon Chain Stations Info

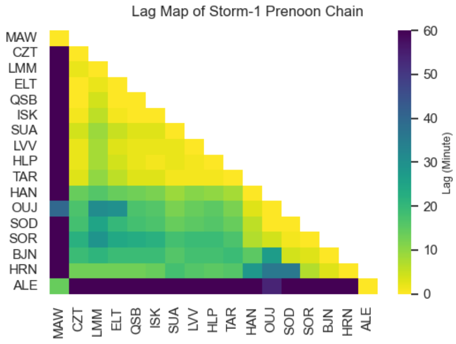

(a) Storm-1 prenoon chain lag

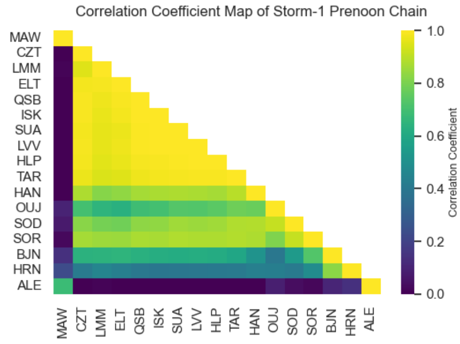

(b) Storm-1 prenoon chain correlation coefficient

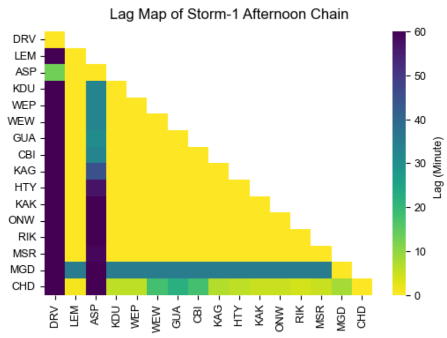

(c) Storm-1 afternoon chain lag

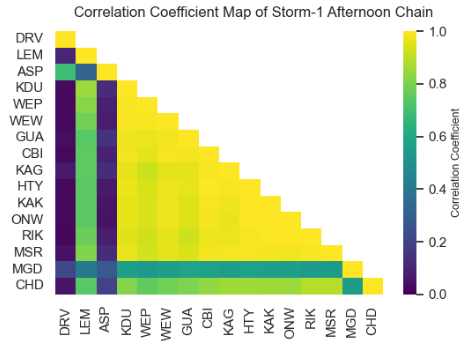

(d) Storm-1 afternoon chain correlation coefficient

Figure 4: Cross Correlation result of Storm-1 prenoon and afternoon chain

In order to investigate the details of how impacts change at different latitudes, four more chains are picked by stations at similar magnetic latitudes but longitudinally distributed as equally as possible around the globe. The four chains are at north-high latitude (near 60°), north-mid latitude (near 40°), equator, and south (below -50°). There is no south-mid latitude chain because of a lack of coverage at in the southern hemisphere. For Storm-1, at the north high-latitude chain [shown in Fig 5, there are localized features between stations that are located close to each other within 1-2 MLT hours. Small lags and high correlations are observed between stations BRW, KAV, ARC, FSP, CNL, BLC, and RAN, which are located from 17:47 to 23:02 MLT, suggesting that the variations occurring in these regions are by the same physics mechanism.

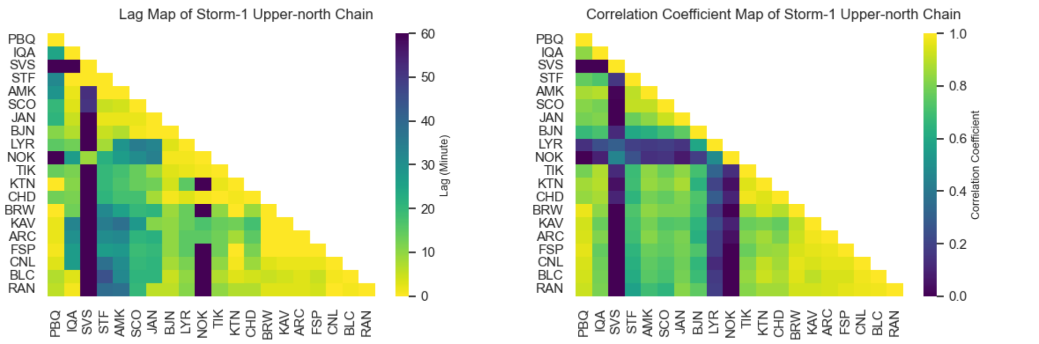

(a) Storm-1 north high-latitude chain lag (b) Storm-1 north high-latitude chain correlation coefficient

Figure 5: Cross Correlation result of Storm-1 north high-latitude chain

In the north mid-latitude chain, the stations on the dayside (NVS, IRT, BMT, PPI, MSR, PET from 11:04 to 15:48 MLT) and night side (VIC, FRN, TUC, BOU, DLR, BSL from 20:26 to 23:23 MLT) are affected by different mechanism as the two sides show higher correlations and smaller lags amongst themselves but aren't related across sides [as shown in Fig 6].

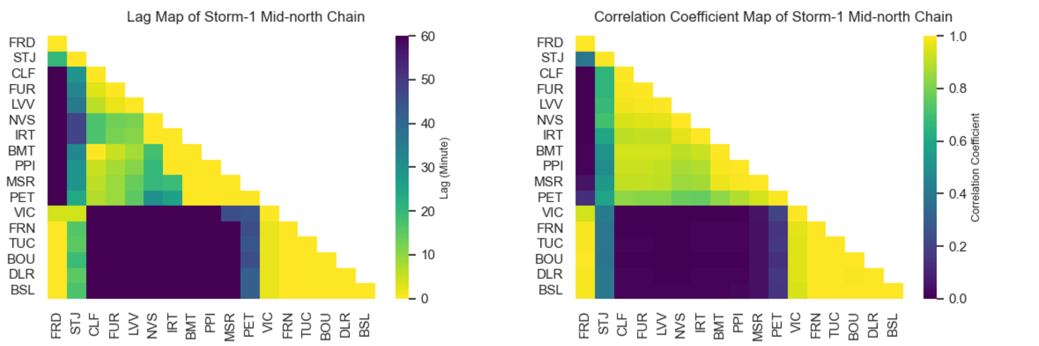

(a) Storm-1 north mid-latitude chain lag (b) Storm-1 north mid-latitude chain correlation coefficient

Figure 6: Cross Correlation result of Storm-1 north mid-latitude chain

In the equator chain, the stations are similarly divided between dayside (MBO, TAM, BNG, MLT, AAE, ABG, PHU, TND, GUA from 04:32 to 15:04 MLT) and nightside (API, HON, PPT, HUA, VRE, KOU from to 18:11 to 02:24 MLT) with high correlation amongst each side but the two show little relationship with each other [as shown in Fig 7].

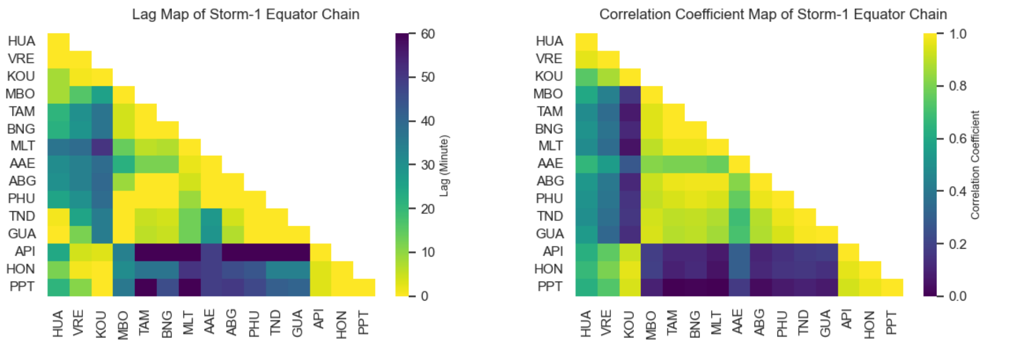

(a) Storm-1 equator chain lag (b) Storm-1 equator chain correlation coefficient

Figure 7: Cross Correlation result of Storm-1 equator chain

Stations from the south high-laitude chain are slightly different. Their correlations are small and lags are high between stations, except for the closely located stations of B03, B23, B14, B15, B04. This is probably due to the high magnitude of the variation [as shown in Fig 8].

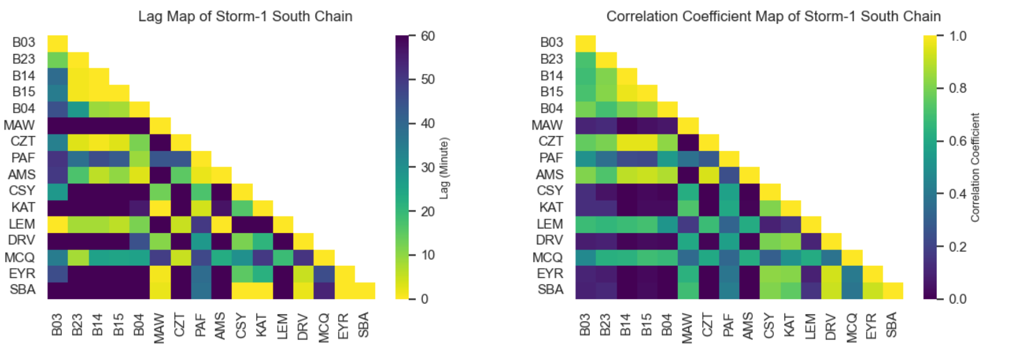

(a) Storm-1 south chain lag (b) Storm-1 south chain correlation coefficient

Figure 8: Cross Correlation result of Storm-1 south chain

For Storm-2, since it happened 12 hours after Storm-1, similar stations are selected as pre-midnight and after-midnight chains shown in Tables 3 and 4. The magnitudes of dBn variations are strong between 55°-75°for the pre-midnight chain, which peaked over 2000 nT at SOD (MagLat 64.0°). As a comparison, the variations of dBn at mid- and low-latitude stations are near 400-600 nT. For the after-midnight chain, the variations at high-latitude stations above 55°are over 1000-2000 nT, while variations at the mid- and low-latitude stations are around 200-300 nT.

As shown in Fig 9 (a) and (b), the colormaps of the lag and correlation at the pre-midnight chain present that variations at HBK, BNG, AAe, QSB, ISK, SUA, and LVV are similar to each other with high correlations and low lag. These stations are located between -36.0°and 40.4°in the mid- and low-latitudes. The correlations decrease at the stations located about 50°, especially for the stations at very high latitudes over 70°such as BJN, HRN, NRD, ALE, and MAW. For the after-midnight chain of Storm-2 present, the high correlation and low lag show global effects in mid- and low-latitude regions, while impacts at high-latitude regions (CHD at MagLat 65.1°, KTN at MagLat 70.4°, DRV at MagLat -80.5°) are the opposite. This could be attributed to the larger intensity of Field Aligned Currents (FACs) at high-latitude regions [as shown in Fig 9 c and d].

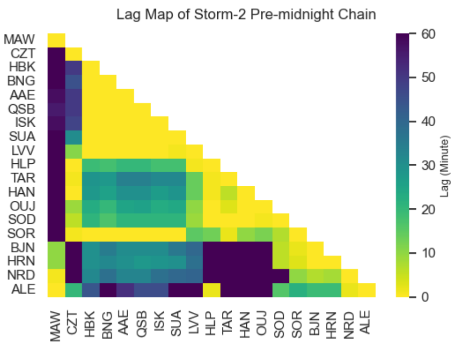

(a) Storm-2 pre-midnight chain lag

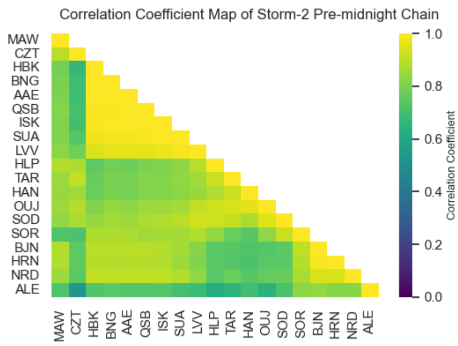

(b) Storm-2 pre-midnight chain correlation coefficient

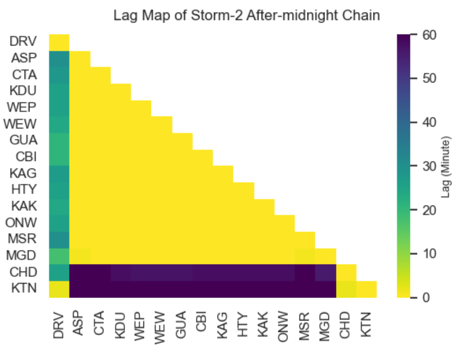

(c) Storm-2 after-midnight chain lag

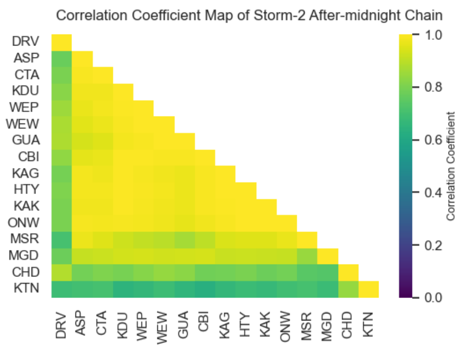

(d) Storm-2 after-midnight chain correlation coefficient

Figure 9: Cross Correlation result of Storm-2 pre-midnight and after-midnight chain

IAGA	**MAGLON**	**MAGLAT**	**MLT**	**Min dBn**	**Max dBn**
MAW	90.3	−70.3	18.9	−1101.3	119.4
CZT	106.2	−53.2	19.9	−1093.9	206.0
HBK	95.3	−36.0	19.2	− 268.2	−106.3
BNG	90.3	− 7.8	18.9	− 402.3	−163.3
AAE	110.7	0.4	20.2	− 367.8	−146.8
QSB	107.4	27.8	20.0	− 357.3	−100.3
ISK	101.5	35.6	19.6	− 293.0	− 77.3
SUA	99.5	40.4	19.5	− 366.7	− 63.5
LVV	98.1	45.5	19.4	− 399.9	− 48.0
HLP	95.0	50.8	19.2	− 794.2	3.0
TAR	102.8	54.5	19.7	−1063.3	254.7
HAN	104.4	58.7	19.8	−1853.2	407.4
OUJ	106.0	61.0	19.9	−1918.1	394.8
SOD	107.1	64.0	20.0	−2035.4	138.4
SOR	105.9	67.4	19.9	−1346.9	3.7
BJN	107.8	71.5	20.0	−1133.9	29.3
HRN	109.0	74.2	20.1	−1046.9	3.6
NRD	103.2	81.1	19.7	− 446.3	92.3
ALE	94.0	87.2	19.1	−1056.9	377.9

Table 3: Pre−midnight Chain Stations Info

IAGA	MAGLON	MAGLAT	MLT	Min dBn	Max dBn
DRV	−124.1	−80.5	4.6	− 953.1	−132.3
ASP	−152.7	−34.0	2.7	− 182.1	57.0
CTA	−139.6	−29.1	3.6	− 209.5	20.1
KDU	−155.2	−21.8	2.5	− 195.4	2.9
WEP	−145.3	−21.4	3.2	− 231.9	− 28.5
WEW	−144.3	−11.6	3.2	− 250.6	− 51.2
GUA	−144.0	6.2	3.3	− 274.3	− 86.8
CBI	−146.4	20.0	3.1	− 218.6	− 33.8
KAG	−157.2	24.8	2.4	− 154.8	30.3
HTY	−148.5	26.2	3.0	− 245.8	24.6
KAK	−148.0	29.4	3.0	− 213.4	20.0
ONW	−146.8	31.6	3.1	− 212.5	28.3
MSR	−146.0	37.7	3.1	− 219.1	117.6
MGD	−140.4	53.9	3.5	−1230.4	− 9.9
CHD	−146.9	65.1	3.1	−2222.7	− 96.3
KTN	−158.2	70.4	2.3	−2507.5	267.7

Table 4: After-midnight Chain Stations Info

In the north high-latitude chain, generally the correlations are high and lags are low for most stations except for ARC, KAV, KTN, NOK. It should be noted that there are very strong impacts at ARC, KAV, KTN, NOK of about 1000 2000 nT, which could be a cause of this deviation [as shown in Fig 10].

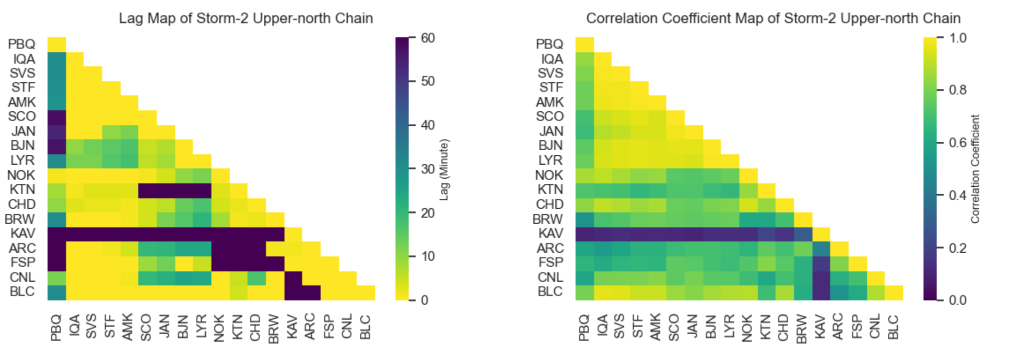

(a) Storm-2 north high-latitude chain lag

(b) Storm-2 north high-latitude chain correlation coefficient

Figure 10: Cross Correlation result of Storm-2 north high-latitude chain

In the north mid-latitude chain, the stations on the dayside (FRD, DLR, BOU, TUC, FRN, VIC) show higher correlations and smaller lags amongst each other; while the stations on the night side (NVS, IRT, BMT, PPI, MSR, PET) also have similar features [as shown in Fig 11].

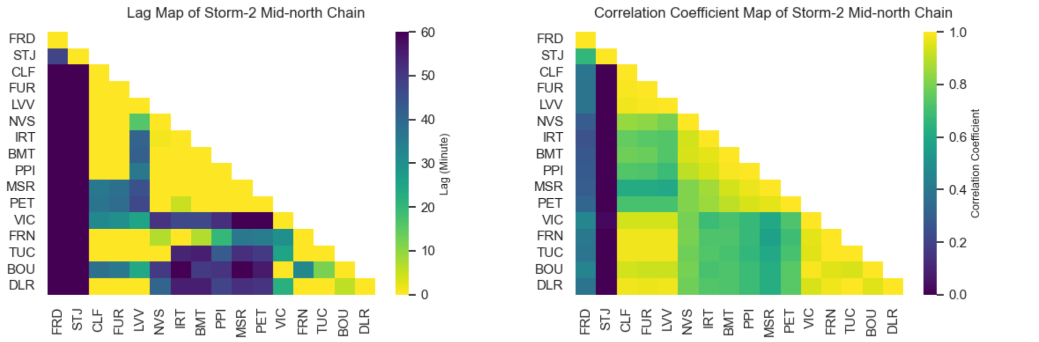

(a) Storm-2 north mid-latitude chain lag (b) Storm-2 north mid-latitude chain correlation coefficient

Figure 11: Cross Correlation result of Storm-2 north mid-latitude chain

The stations from the equator chain have high correlations and the lags are 0, which shows that there is a global impact at the equator regions. This is due to the small impacts of Storm-2 at the equator regions, with variation only reaching 100 nT [as shown in Fig 12].

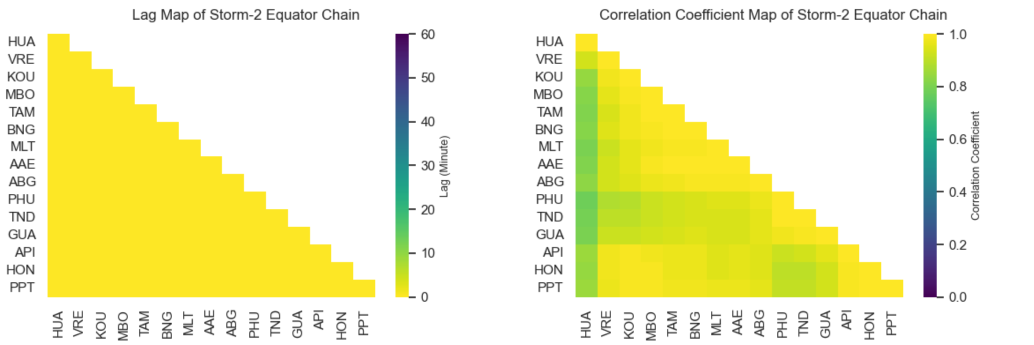

(a) Storm-2 equator chain lag (b) Storm-2 equator chain correlation coefficient

Figure 12: Cross Correlation result of Storm-2 equator chain

The stations in the south chain present little correlation and high lags except for the closely located stations of B23, B14, B15, B04. This suggests that the variations these stations recorded have different drivers [as shown in Fig 13].

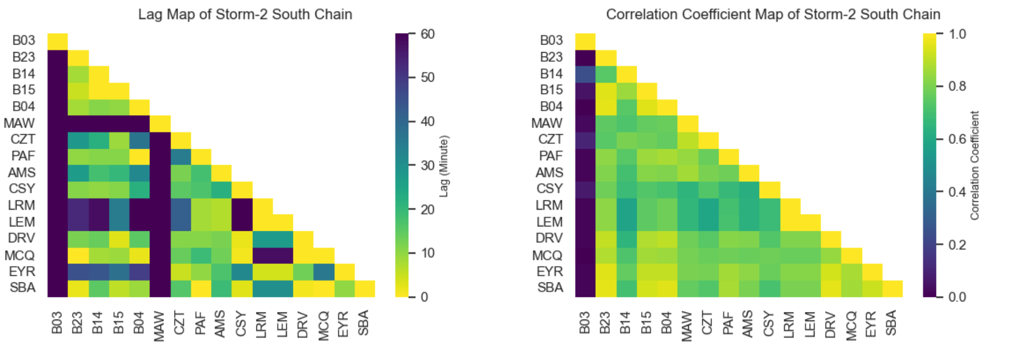

(a) Storm-2 south chain lag

(b) Storm-2 south chain correlation coefficient

Figure 13: Cross Correlation result of Storm-2 south chain

4 Discussion and Conclusion

The results of the global maps show that impacts at high latitudes occurred first for Storm-1 and 2 on 29 October 2003 Halloween Storm. Then, the regions of impact expanded from high-latitude to mid- and low latitudes. Aurorae were observed at mid- and low-latitudes as far south as Texas and the Mediterranean countries of Europe. The first impact located at high-latitude regions can be explained by the southward IMF (shown in Fig 1) leading to magnetic field reconnection and energy and particles are transported to polar regions first (Kamide, 2006) (Tóth et al., 2007). The physics mechanism of magnetic field variations can be explained by current systems associated with the growth, expansion, and recovery phases of substorms (Akasofu, 2007).

The results of the global maps show that high latitudes between 55°and 75°are the most intense regions of impact for Storm-1 and 2. The dBn value was as low as -2800nT near B15 (MagLong 36.7°, MagLat -68.6°) in high-latitude regions for Storm-1. For Storm-2, it is -2500 nT near MCQ (MagLong -111.74, MagLat -64.39). As one of the regions of impacts shown by the global maps, the Sydkraft utility group in Sweden reported that strong GICs over Northern Europe caused transformer problems and even a system failure and subsequent blackout. During the expansion to mid- and low-latitude periods, the north of Spain experienced an intensity of impact of about -800 nT in the northern hemisphere, and South Africa experienced -900 nT of impact in the southern hemisphere. Twelve transformers in South Africa were disabled and had to be replaced. These results matched the previous study carried by (Woodroffe et al., 2016), in which it shows that the most intensive impacts are located at high magnetic latitude regions. The variations of magnetic field vary from 700 nT at 45-50 degree of magnetic latitude to 2800 nT at 60-65 degree.

The cross-correlation results show that localized patterns occur more in the high-latitude regions and the regions of more intensive impacts, such as the pre-noon chain in Storm-1, pre-midnight chain in Storm-2, and high-latitude chains in both Storms, because the dynamics of energy and particle inputs are associated with localized field-aligned currents (FACs) at these regions. The global patterns occur more in the mid and equatorial regions and these regions show less intensive impacts, such as the afternoon chain in Storm-1, after-midnight chain in Storm-2, and equatorial chains in both storms, because the impacts from large-scale variations of currents (ring currents, magnetopause currents) are not as strong as localized FACs and other features near ground.

Due to the data availability and coverage, the global maps and cross-correlation analysis of latitudinal and longitudinal chains can provide information over large spatial grids. The limitation of kriging interpolation depends on the distance between nodes. To provide better space weather information, it urges the development of better and more dense spatial and temporal coverage of magnetometer observations. To cover the fine localized dynamics of possible GIC impacts, 100 km by 100 km spatial coverage with 1-second temporal resolution will be ideal.

As the conclusion of research paper, the global map presents a big picture that shows where the impacts first occur on the Earth, how the regions of impact expanded, and how intense the impacts were. The regions with strong impacts, such as Sweden, and South Africa, had experienced power outages over hours. The global and local feature analysis carried out by cross-correlation study shows that the intensive impacts are associated with more dynamic and localized features. To provide better space weather impacts and to improve the understanding of space weather mechanisms, it urges the development of better magnetometers or other space weather observations in both spatial and temporal domains. The global view of space weather impacts can help us to understand and mitigate the hazardous impacts on modern society. The visualization package is developed and available on GITHUB. It could be used by the space weather community. The researchers who work on space weather predictions could use the codes to generate the maps of predicted geomagnetic field variations and compare them with the observed global maps of geomagnetic field variations, to verify whether the predictions match the observation and how to improve the model to get better and more accurate results.

In the future, with more spatial coverage of magnetometer observations, the global maps could show detailed regional impacts at 100 km by 100 km grid scales. Combining the maps with other GIS information databases could provide the space weather impact estimation not only on power grid operations, but also on other crucial infrastructures, including hospitals, financial centers, emergency response, and national security-related agencies. During the last decade, the US government has developed a series of government reports and national action plans (*National Space Weather Strategy and Action Plan*, 2019) on space weather operations with multiple agencies, including NSF, NASA, FEMA, National Science and Technology Council, National Security Council, Office of Science and Technology Policy, DoC, DoE, DoD, and others. The importance of space weather has been promoted to the national strategic level. The research on space weather impact will make more and more valuable contributions with the coming of the space era.

5 Open Research

The global map model, the correlation map model, the code used to generate these models, and the data used are all available at GitHub via `https://github.com/PythonOrC/SpaceWeather` with GNU General Public License v3.0. An archive of this can be found in this citation (Hu, 2023). Matlab (Inc., 2022) was used to generate the global map model frames, and the GIF was synthesized with Python and the Pillow module (Clark, 2015). The correlation map was generated with Python and the following modules: pandas(pandas development team, 2020; Wes McKinney, 2010), numpy(Harris et al., 2020), matplotlib(Hunter, 2007), seaborn(Waskom, 2021). The ground magnetometer data used in this research was provided by SuperMAG(Gjerloev, 2012; SuperMAG, 2009). The ACE data used in this study was provided by The Solar and Heliospheric Observatory (SOHO)(The Solar and Heliospheric Observatory (SOHO) Project Scientist Team, 2018). The SYM_H data used in this paper was provided by the WDC for Geomagnetism, Kyoto (`http://wdc.kugi.kyoto-u.ac.jp/wdc/Sec3.html`)(World Data Center for Geomagnetism, Kyoto, 2018; S et al., 2022).

Acknowledgments

For the ground magnetometer data, we gratefully acknowledge the SuperMAG (`https://supermag.jhuapl.edu/info/?page=acknowledgement`) and its collaborators: INTERMAG-

NET, Alan Thomson; CARISMA, PI Ian Mann; CANMOS, Geomagnetism Unit of the Geological Survey of Canada; The S-RAMP Database, PI K. Yumoto and Dr. K. Shiokawa; The SPIDR database; AARI, PI Oleg Troshichev; The MACCS program, PI M. Engebretson; GIMA; MEASURE, UCLA IGPP and Florida Institute of Technology; SAMBA, PI Eftyhia Zesta; 210 Chain, PI K. Yumoto; SAMNET, PI Farideh Honary; IMAGE, PI Liisa Juusola; Finnish Meteorological Institute, PI Liisa Juusola; Sodankylä Geophysical Observatory, PI Tero Raita; UiT the Arctic University of Norway, Tromsø Geophysical Observatory, PI Magnar G. Johnsen; GFZ German Research Centre For Geosciences, PI Jürgen Matzka; Institute of Geophysics, Polish Academy of Sciences, PI Anne Neska and Jan Reda; Polar Geophysical Institute, PI Alexander Yahnin and Yarolav Sakharov; Geological Survey of Sweden, PI Gerhard Schwarz; Swedish Institute of Space Physics, PI Masatoshi Yamauchi; AUTUMN, PI Martin Connors; DTU Space, Thom Edwards and PI Anna Willer; South Pole and McMurdo Magnetometer, PI's Louis J. Lanzarotti and Alan T. Weatherwax; ICESTAR; RAPIDMAG; British Artarctic Survey; McMac, PI Dr. Peter Chi; BGS, PI Dr. Susan Macmillan; Pushkov Institute of Terrestrial Magnetism, Ionosphere and Radio Wave Propagation (IZMIRAN); MFGI, PI B. Heilig; Institute of Geophysics, Polish Academy of Sciences, PI Anne Neska and Jan Reda; University of L'Aquila, PI M. Vellante; BCMT, V. Lesur and A. Chambodut; Data obtained in cooperation with Geoscience Australia, PI Andrew Lewis; AALPIP, co-PIs Bob Clauer, Michael Hartinger, and Zhonghua Xu; MagStar, PI Jennifer Gannon; SuperMAG, PI Jesper W. Gjerloev; Data obtained in cooperation with the Australian Bureau of Meteorology, PI Richard Marshall. For the solar wind and IMF data, we gratefully acknowledge NASA Solar and Heliospheric Observatory (SOHO) Project website (`https://sohoftp.nascom.nasa.gov/sdb/goes/ace/daily/`).

Appendix A Table of All Stations Used and Related Information

IAGA	GEOLON	GEOLAT	MAGLON	MAGLAT
AAE	38.77	9.03	110.68	0.42
ABG	72.87	18.62	145.39	12.09
ABK	18.82	68.35	101.53	65.31
AIA	295.74	-65.25	9.11	-50.28
ALE	297.5	82.5	94	87.16
AMK	322.37	65.6	53.63	69.05
AMS	77.57	-37.8	138.9	-49.14
AND	16.03	69.3	100.1	66.45
API	188.22	-13.8	-97.37	-15.58
AQU	13.32	42.38	87.29	36.34
ARC	214.44	68.12	-96.08	68.83
ASC	345.62	-7.95	56.11	-15.2
ASP	133.88	-23.77	-152.74	-34.04
ATU	306.43	67.93	38.14	74.2
B03	291.88	-67.57	7.64	-52.47
B04	41.08	-68.58	73.64	-66.18
B11	336.58	-77.51	30.11	-63.47
B12	335.88	-79.08	29.1	-64.7
B14	337.74	-80.89	28.8	-66.31
B15	2.97	-81.49	36.66	-68.6
B17	347.76	-82.9	30.3	-68.53
B18	336.14	-84.35	25.78	-69.17
B19	2.06	-85.36	29.96	-71.17
B20	95.98	-85.36	30.09	-77.75
B21	28.41	-87	28.91	-73.39
B22	68.17	-86.51	30.66	-75.54
B23	316.13	-88.03	19.78	-72.18
BDV	14.02	49.07	89.32	44.57
BEL	20.8	51.83	95.93	47.67
BET	208.45	66.9	-100	66.55
BFE	11.67	55.62	89.31	52.12
BJN	19.2	74.5	107.77	71.51
BLC	263.99	64.32	-31.98	73.76
BMT	116.2	40.3	-171	34.7
BNG	18.57	4.33	90.32	-7.75
BOU	254.76	40.14	-40.05	48.93
BRW	203.38	71.32	-108.13	70.21
BSL	270.36	30.35	-19.21	41.22
CAN	149.36	-35.31	-133.08	-45.32

IAGA	GEOLON	GEOLAT	MAGLON	MAGLAT
CBB	254.97	69.12	-50.3	77.08
CBI	142.3	27.15	-146.38	19.99
CCS	104.28	77.72	175.87	72.2
CER	289.4	-33.45	0.67	-20.22
CHD	147.89	70.62	-146.94	65.13
CLF	2.27	48.02	79.15	43.53
CMO	212.14	64.87	-95.41	65.14
CNB	150.7	-34.1	-131.84	-43.83
CNL	248.75	65.75	-56.62	73.05
CSY	110.53	-66.28	156.87	-80.78
CTA	146.3	-20.1	-139.56	-29.11
CUL	149.58	-30.28	-134.06	-39.82
CZT	51.87	-46.43	106.22	-53.2
DAW	220.89	64.05	-87.04	65.99
DLR	259.08	29.49	-33.4	38.82
DMH	341.37	76.77	85.13	77.2
DNB	339.78	74.3	78.89	75.06
DOB	9.11	62.07	90	59.29
DOU	4.6	50.1	81.65	46.03
DRV	140.01	-66.67	-124.11	-80.5
EAG	218.84	64.78	-89.46	66.32
EBR	0.49	40.82	76.07	33.86
ELT	34.95	29.67	106.57	22.73
ESK	356.8	55.32	77.09	52.75
EWA	202	21.32	-90.01	21.37
EYR	172.4	-43.4	-103.47	-50.06
FCC	265.91	58.76	-27.24	68.75
FHB	310.32	62	38.89	67.62
FIT	279.05	28.07	-7.69	39.31
FMC	248.79	56.66	-51.71	64.36
FRD	282.63	38.2	-1.83	48.85
FRN	240.28	37.09	-56.15	42.98
FSP	238.77	61.76	-66.72	67.38
FUR	11.28	48.17	86.74	43.52
FYU	214.78	66.56	-94.43	67.33
GAK	214.87	62.39	-91.43	63.14
GDH	306.47	69.25	39.4	75.45
GIM	265.36	56.38	-27.68	66.44
GLN	262.88	49.65	-30.45	59.66
GUA	144.87	13.59	-144.04	6.17
GUI	343.57	28.32	60.53	16.49

IAGA	GEOLON	GEOLAT	MAGLON	MAGLAT
GZH	113.34	23.09	-174.75	16.44
HAD	355.52	50.98	74.53	47.66
HAN	26.6	62.25	104.39	58.68
HBK	27.71	-25.88	95.28	-35.96
HER	19.23	-34.43	82.83	-42.28
HLP	18.82	54.61	95	50.77
HOB	147.35	-42.88	-133.2	-53.89
HON	202	21.32	-90.01	21.37
HOR	15.6	77	108.98	74.17
HRB	18.19	47.86	92.68	43.15
HRN	15.6	77	108.98	74.17
HTY	139.8	33.12	-148.49	26.17
HUA	284.67	-12.05	-3.57	0.4
IQA	291.48	63.75	14.85	72.54
IRT	104.45	52.17	177.49	47.48
ISK	29.06	41.07	101.53	35.59
ISL	265.34	53.86	-27.34	64.02
IVA	27.29	68.56	108.38	65.14
JAN	351.3	70.9	82.94	70.24
KAG	130.72	31.48	-157.16	24.8
KAK	140.18	36.23	-148.04	29.35
KAT	117.62	-33.68	-171.03	-46.09
KAV	216.35	70.14	-96.53	71.15
KDU	132.47	-12.69	-155.21	-21.81
KEV	27.01	69.76	109.02	66.37
KIL	20.77	69.06	103.59	65.94
KIR	20.42	67.84	102.43	64.7
KNY	130.88	31.42	-157	24.73
KOU	307.27	5.21	23.53	9.45
KTN	137.71	75.94	-158.19	70.4
KUV	302.82	74.57	42.42	80.91
LEM	147.5	-42.3	-133.21	-53.23
LER	358.82	60.13	80.82	57.99
LMM	32.58	-25.92	100.12	-35.87
LOV	17.83	59.35	95.85	55.92
LRM	115	-21	-173.24	-31.73
LRV	338.3	64.18	66.75	64.91
LVV	23.75	49.9	98.08	45.51
LYR	15.83	78.2	111.39	75.3
LZH	103.85	36.09	176.31	30.58
MAB	5.68	50.3	82.6	46.23

IAGA	GEOLON	GEOLAT	MAGLON	MAGLAT
MAS	23.7	69.46	106.18	66.21
MAW	62.88	-67.61	90.27	-70.25
MBO	343.03	14.38	57.82	1.31
MCM	166.67	-77.85	-32.9	-79.92
MCQ	158.95	-54.5	-111.74	-64.39
MEA	246.65	54.62	-53.74	61.94
MGD	150.86	59.97	-140.35	53.9
MLT	30.89	29.52	102.5	21.93
MMB	144.19	43.91	-144.33	37.13
MSR	142.27	44.37	-146.03	37.66
MUO	23.53	68.02	105.01	64.74
MUT	121.02	14.37	-167.38	7.21
NAL	11.95	78.92	110.45	76.24
NAQ	314.56	61.16	43.08	65.93
NCK	16.72	47.63	91.33	42.87
NEW	242.88	48.27	-56.3	54.81
NGK	12.68	52.07	89	48.08
NOK	88.1	69.4	161.98	64.86
NRD	343.33	81.6	103.17	81.08
NUR	24.65	60.5	102.03	56.91
NVS	82.9	55.03	155.72	50.86
ONW	141.47	38.43	-146.8	31.57
OSO	286.91	-40.34	-0.49	-26.59
OTT	284.45	45.4	1.43	55.66
OUJ	27.23	64.52	105.97	61.01
PAC	289.91	-40.34	1.52	-26.69
PAF	70.26	-49.35	122.32	-58.57
PBK	170.9	70.08	-129.92	65.4
PBQ	282.26	55.28	-0.94	65.47
PEL	24.08	66.9	104.72	63.57
PET	158.25	52.97	-133.12	46.49
PHU	105.95	21.03	177.86	14.17
PIN	263.96	50.2	-28.94	60.33
PKR	212.57	65.12	-95.22	65.48
PNT	289.1	-53.2	2.75	-38.7
PPI	131.73	42.98	-155.7	36.69
PPT	210.42	-17.57	-74.62	-16.66
PST	302.11	-51.7	10.5	-38.31
PUT	290.5	-18.33	1.56	-5.93
QSB	35.64	33.87	107.42	27.75
RAL	256.32	58.22	-41.82	67.14

IAGA	GEOLON	GEOLAT	MAGLON	MAGLAT
RAN	267.89	62.82	-24.87	72.67
RES	265.11	74.69	-39.08	83.08
RIK	143.76	43.48	-144.7	36.7
RVK	10.99	64.94	93.11	62.22
SBA	166.78	-77.85	-32.9	-79.9
SCO	338.03	70.48	72.06	71.51
SER	288.87	-30	0.13	-16.93
SIT	224.67	57.06	-79.4	59.76
SJG	293.85	18.11	10.68	27.69
SKT	307.1	65.42	37.09	71.64
SMI	248.07	60.03	-54.08	67.51
SOD	26.63	67.37	107.07	63.95
SOR	22.22	70.54	105.9	67.37
SPA	0	-90	18.94	-74.1
SPT	355.65	39.55	71.88	32.06
STF	309.28	67.02	40.84	72.82
STJ	307.32	47.6	31.19	53.22
SUA	26.25	45.32	99.48	40.38
SVS	294.9	76.02	33.27	83.29
TAL	266.45	69.54	-30.27	78.68
TAM	5.53	22.79	78.33	9.43
TAN	47.55	-18.92	116.86	-28.71
TAR	26.46	58.26	102.76	54.51
TEO	260.82	19.75	-30.48	29
THL	290.77	77.47	29.74	85.03
THY	17.54	46.9	91.89	42.02
TIK	128.92	71.59	-162.33	66.14
TND	124.95	1.29	-163.48	-6.59
TRO	18.94	69.66	102.64	66.65
TRW	294.68	-43.25	4.91	-29.77
TSU	17.7	-19.22	86.99	-30.48
TUC	249.27	32.17	-45.16	39.76
UMQ	307.87	70.68	42.73	76.57
UPN	303.85	72.78	40.45	79.15
UPS	17.35	59.9	95.68	56.53
VAL	349.75	51.93	70.23	49.39
VIC	236.58	48.52	-63.52	53.73
VLD	286.86	-39.48	-0.62	-25.78
VRE	292.38	-17.28	3.29	-5.19
VSS	316.35	-22.4	23.13	-17.96
WEP	141.88	-12.68	-145.27	-21.42

IAGA	GEOLON	GEOLAT	MAGLON	MAGLAT
WEP	141.88	-12.68	-145.27	-21.42
WEW	143.62	-3.55	-144.3	-11.56
WNG	9.07	53.75	86.5	50.13
YKC	245.52	62.48	-58.77	69.39

References

Akasofu, S.-I. (2007). *Exploring the secrets of the aurora.* Springer Netherlands. Retrieved from `https://link.springer.com/book/10.1007/0-306-47970-2`

Baker, D., Balstad, R., Bodeau, M., Cameron, E., Fennell, J., Forbes, K., ... Strachan, L. (2008). *Severe space weather events: Understanding societal and economic impacts: A workshop report.* Washington, DC: The National Academies Press. Retrieved from `https://nap.nationalacademies.org/catalog/12507/severe-space-weather-events-understanding-societal-and-economic-impacts-a` doi: 10.17226/12507

Barbosa, C. S., Alves, L. R., Caraballo, R., Hartmann, G. A., Papa, A. R. R., & Pirjola, R. J. (2015). Analysis of geomagnetically induced currents at a low-latitude region over the solar cycles 23 and 24: comparison between measurements and calculations. *Journal of Space Weather and Space Climate*, *5*.

Batista, I. S., Abdu, M. A., de Souza, J. R., Bertoni, F. C. P., Matsuoka, M. T., de Oliveira Camargo, P., & Bailey, G. J. (2006). Unusual early morning development of the equatorial anomaly in the brazilian sector during the halloween magnetic storm. *Journal of Geophysical Research*, *111*, 10.

Belakhovsky, V. B., Pilipenko, V. A., Engebretson, M. J., Sakharov, Y., & Selivanov, V. (2019). Impulsive disturbances of the geomagnetic field as a cause of induced currents of electric power lines. *Journal of Space Weather and Space Climate*.

Belakhovsky, V. B., Pilipenko, V. A., Sakharov, Y. A., & Selivanov, V. (2018). Characteristics of the variability of a geomagnetic field for studying the impact of the magnetic storms and substorms on electrical energy systems. *Izvestiya, Physics of the Solid Earth*, *54*, 52-65.

Berger, T. E., Holzinger, M. J., Sutton, E. K., & Thayer, J. P. (2020). Flying through uncertainty. *Space Weather*, *18*(1), e2019SW002373. Retrieved from `https://agupubs.onlinelibrary.wiley.com/doi/abs/10.1029/2019SW002373` (e2019SW002373 2019SW002373) doi: https://doi.org/10.1029/2019SW002373

Boteler, Pirjola, R., & Nevanlinna, H. (1998). The effects of geomagnetic disturbances on electrical systems at the earth's surface. *Advances in Space Research*, *22*(1), 17-27. Retrieved from `https://www.sciencedirect.com/science/article/pii/S027311779701096X` (Solar-Terrestrial Relations: Predicting the Effects on the Near-Earth Environment) doi: https://doi.org/10.1016/S0273-1177(97)01096-X

Boteler, D. H. (2019). A 21st century view of the march 1989 magnetic storm. *Space Weather*, *17*(10), 1427-1441. Retrieved from `https://agupubs.onlinelibrary.wiley.com/doi/abs/10.1029/2019SW002278` doi: https://doi.org/10.1029/2019SW002278

Buck, J. R., Daniel, M. M., & Singer, A. C. (2002). *Computer explorations in signals and systems using matlab, 2e.* Retrieved from `https://www.mathworks.com/academia/books/computer-explorations-in-signals-and-systems-using-matlab-buck.html`

Clark, A. (2015). *Pillow (pil fork) documentation.* readthedocs. Retrieved from `https://buildmedia.readthedocs.org/media/pdf/pillow/latest/pillow.pdf`

Dimmock, A. P., Rosenqvist, L., Hall, J.-O., Viljanen, A., Yordanova, E., Honkonen, I., ... Sjöberg, E. C. (2019). The gic and geomagnetic response over fennoscandia to the 7–8 september 2017 geomagnetic storm. *Space Weather*, *17*, 1010 - 989.

Eastwood, J. P., Biffis, E., Hapgood, M. A., Green, L., Bisi, M. M., Bentley, R. D., ... Burnett, C. (2017). The economic impact of space weather: Where do we stand? *Risk Analysis*, *37*(2), 206-218. Retrieved from `https://onlinelibrary.wiley.com/doi/abs/10.1111/risa.12765` doi: https://doi.org/10.1111/risa.12765

Ebihara, Y., ichi Watari, S., & Kumar, S. (2021). Prediction of geomagnetically induced currents (GICs) flowing in japanese power grid for carrington-class magnetic storms. *Earth, Planets and Space*, *73*, 1-10.

Engebretson, M. J., Pilipenko, V. A., Ahmed, L. Y., Posch, J. L., Steinmetz, E. S., Moldwin, M. B., ... Vorobev, A. V. (2019). Nighttime magnetic perturbation events observed in arctic canada: 1. survey and statistical analysis. *Journal of Geophysical Research: Space Physics*, *124*, 7442 - 7458.

Engebretson, M. J., Pilipenko, V. A., Steinmetz, E. S., Moldwin, M. B., Connors, M. G., Boteler, D. H., ... Russell, C. T. (2020). Nighttime magnetic perturbation events observed in arctic canada: 3. occurrence and amplitude as functions of magnetic latitude, local time, and magnetic disturbance indices. *Space Weather*, *19*.

FEMA Homeland Security. (2019, May). Federal Operating Concept for Impending Space Weather Events.

Forbes, T. G. (2000). A review on the genesis of coronal mass ejections. *Journal of Geophysical Research: Space Physics*, *105*(A10), 23153-23166. doi: 10.1029/2000JA000005

Gannon, J. (2019). *Geomagnetically induced currents from the sun to the power grid* (J. L. Gannon, A. Swidinsky, & Z. Xu, Eds.). Nashville, TN: John Wiley & Sons.

Gjerloev, J. W. (2012). The supermag data processing technique. *Journal of Geophysical Research: Space Physics*, *117*(A9). Retrieved from `https://agupubs.onlinelibrary.wiley.com/doi/abs/10.1029/2012JA017683` doi: https://doi.org/10.1029/2012JA017683

Harris, C. R., Millman, K. J., van der Walt, S. J., Gommers, R., Virtanen, P., Cournapeau, D., ... Oliphant, T. E. (2020, September). Array programming with NumPy. *Nature*, *585*(7825), 357–362. Retrieved from `https://doi.org/10.1038/s41586-020-2649-2` doi: 10.1038/s41586-020-2649-2

Hathaway, D. H., & Wilson, R. M. (2006). Geomagnetic activity indicates large amplitude for sunspot cycle 24. *Geophysical Research Letters*, *33*.

Hood, A. W., & Priest, E. R. (1979, December). Kink instability of solar coronal loops as the cause of solar flares. *Solar Physics*, *64*(2), 303–321. Retrieved from `https://doi.org/10.1007/BF00151441` doi: 10.1007/BF00151441

Hu, H. (2023, April). *Investigating the Space Weather Impact of the 2003 Halloween Geomagnetic Storm by the Ground Magnetic Field Variations: a Global View.* Zenodo. Retrieved from `https://doi.org/10.5281/zenodo.7830370` (If you use this software, please cite it as below.) doi: 10.5281/zenodo.7830370

Hunter, J. D. (2007). Matplotlib: A 2d graphics environment. *Computing in Science & Engineering*, *9*(3), 90–95. doi: 10.1109/MCSE.2007.55

Inc., T. M. (2022). *Matlab version: 9.13.0 (r2022b).* Natick, Massachusetts, United States: Author Retrieved from `https://www.mathworks.com`

Kamide, Y. (2006). What is an "intense geomagnetic storm"? *Space Weather*, *4*(6). Retrieved from `https://agupubs.onlinelibrary.wiley.com/doi/abs/10.1029/2006SW000248` doi: https://doi.org/10.1029/2006SW000248

Knipp, D. J. (2015). Synthesis of geomagnetically induced currents: Commentary and research. *Space Weather*, *13*(11), 727-729. Retrieved from `https://agupubs.onlinelibrary.wiley.com/doi/abs/10.1002/2015SW001317` doi: https://doi.org/10.1002/2015SW001317

Kotzé, P. B., Cilliers, P. J., & Sutcliffe, P. R. (2015). The role of sansa's geomagnetic observation network in space weather monitoring: A review. *Space Weather*, *13*(10), 656-664. Retrieved from `https://agupubs.onlinelibrary.wiley.com/doi/abs/10`

.1002/2015SW001279 doi: https://doi.org/10.1002/2015SW001279

Kusano, K., Bamba, Y., Yamamoto, T. T., Iida, Y., Toriumi, S., & Asai, A. (2012, oct). MAGNETIC FIELD STRUCTURES TRIGGERING SOLAR FLARES AND CORONAL MASS EJECTIONS. *The Astrophysical Journal*, *760*(1), 31. Retrieved from https://doi.org/10.1088%2F0004-637x%2F760%2F1%2F31 doi: 10.1088/0004-637x/760/1/31

Kusano, K., Maeshiro, T., Yokoyama, T., & Sakurai, T. (2004). The trigger mechanism of solar flares in a coronal arcade with reversed magnetic shear. *The Astrophysical Journal*, *610*, 537 - 549.

Love, J. J., Lucas, G. M., Kelbert, A., & Bedrosian, P. A. (2018). Geoelectric hazard maps for the mid-atlantic united states: 100 year extreme values and the 1989 magnetic storm. *Geophysical Research Letters*, *45*(1), 5-14. Retrieved from https://agupubs.onlinelibrary.wiley.com/doi/abs/10.1002/2017GL076042 doi: https://doi.org/10.1002/2017GL076042

Marshall, R. A., Dalzell, M., Waters, C. L., Goldthorpe, P., & Smith, E. A. (2012). Geomagnetically induced currents in the new zealand power network. *Space Weather*, *10*(8). Retrieved from https://agupubs.onlinelibrary.wiley.com/doi/abs/10.1029/2012SW000806 doi: https://doi.org/10.1029/2012SW000806

Maus, S., & Lühr, H. (2005). Signature of the quiet-time magnetospheric magnetic field and its electromagnetic induction in the rotating earth. *Geophysical Journal International*, *162*(3), 755-763. Retrieved from https://onlinelibrary.wiley.com/doi/abs/10.1111/j.1365-246X.2005.02691.x doi: https://doi.org/10.1111/j.1365-246X.2005.02691.x

Mcallister, A. H., Dryer, M., Mclntosh, P. S., Singer, H. J., & Weiss, L. A. (1996). A large polar crown coronal mass ejection and a "problem" goemagnetic storm: April 14–23, 1994. *Journal of Geophysical Research: Space Physics*, *101*, 13497 - 13515.

National Space Weather Strategy and Action Plan. (2019, March). Retrieved from https://trumpwhitehouse.archives.gov/wp-content/uploads/2019/03/National-Space-Weather-Strategy-and-Action-Plan-2019.pdf

Ngwira, C. M., Pulkkinen, A., Bernabeu, E., Eichner, J. F., Viljanen, A., & Crowley, G. (2015). Characteristics of extreme geoelectric fields and their possible causes: Localized peak enhancements. *Geophysical Research Letters*, *42*, 6916 - 6921.

Ngwira, C. M., Pulkkinen, A., Wilder, F. D., & Crowley, G. (2013). Extended study of extreme geoelectric field event scenarios for geomagnetically induced current applications. *Space Weather*, *11*, 121 - 131.

Orr, L., Chapman, S. C., & Beggan, C. D. (2021). Wavelet and network analysis of magnetic field variation and geomagnetically induced currents during large storms. *Space Weather*, *19*(9), e2021SW002772. Retrieved from https://agupubs.onlinelibrary.wiley.com/doi/abs/10.1029/2021SW002772 (e2021SW002772 2021SW002772) doi: https://doi.org/10.1029/2021SW002772

Osella, A., Favetto, A., & López, E. (1998). Currents induced by geomagnetic storms on buried pipelines as a cause of corrosion. *Journal of Applied Geophysics*, *38*(3), 219-233. Retrieved from https://www.sciencedirect.com/science/article/pii/S0926985197000190 doi: https://doi.org/10.1016/S0926-9851(97)00019-0

pandas development team, T. (2020, February). *pandas-dev/pandas: Pandas.* Zenodo. Retrieved from https://doi.org/10.5281/zenodo.3509134 doi: 10.5281/zenodo.3509134

Pulkkinen, A., Bernabeu, E., Thomson, A., Viljanen, A., Pirjola, R., Boteler, D., ... MacAlester, M. (2017). Geomagnetically induced currents: Science, engineering, and applications readiness. *Space Weather*, *15*(7), 828-856. Retrieved from https://agupubs.onlinelibrary.wiley.com/doi/abs/10.1002/2016SW001501 doi: https://doi.org/10.1002/2016SW001501

S, I., A, M., H, T., & T, I. (2022). *Mid-latitude geomagnetic indices asy and sym (asy/sym indices)* [database]. World Data Center for Geomagnetism, Kyoto. Retrieved from https://wdc.kugi.kyoto-u.ac.jp/aeasy/index.html doi: 10.14989/267216

Schultz, C. (2012). Solar storms can destabilize power grids at midlatitudes. *Eos, Transactions American Geophysical Union*, *93*(41), 412-412. Retrieved from https://agupubs.onlinelibrary.wiley.com/doi/abs/10.1029/2012EO410020 doi: https://doi.org/10.1029/2012EO410020

Shibata, K., & Magara, T. (2011). Solar flares: Magnetohydrodynamic processes. *Living Reviews in Solar Physics*, *8*, 1-99.

Shiokawa, K. (2023). Introduction of space weather research on magnetosphere and ionosphere of the earth. In K. Kusano (Ed.), *Solar-terrestrial environmental prediction* (pp. 95–113). Singapore: Springer Nature Singapore. Retrieved from https://doi.org/10.1007/978-981-19-7765-7_4 doi: 10.1007/978-981-19-7765-7_4

Simpson, F., & Bahr, K. (2020). Estimating the electric field response to the halloween 2003 and september 2017 magnetic storms across scotland using observed geomagnetic fields, magnetotelluric impedances and perturbation tensors. *Journal of Space Weather and Space Climate*, *10*(1), 48-. Retrieved from http://www.sciengine.com/publisher/EDPSciences/journal/JournalofSpaceWeatherandSpaceClimate/10/1/10.1051/swsc/2020049 doi: https://doi.org/10.1051/swsc/2020049

Srivastava, N., & Venkatakrishnan, P. (2002). Relationship between cme speed and geomagnetic storm intensity. *Geophysical Research Letters*, *29*(9), 1-1-1-4. Retrieved from https://agupubs.onlinelibrary.wiley.com/doi/abs/10.1029/2001GL013597 doi: https://doi.org/10.1029/2001GL013597

Stoica, P., & Moses, R. L. (2005). *Spectral analysis of signals*. Pearson/Prentice Hall.

SuperMAG. (2009). [database]. Retrieved from https://supermag.jhuapl.edu/mag/?fidelity=low&start=2003-10-29T00\%3A00\%3A00.000Z&interval=23\%3A59&tab=customdownload&stations=YKC,CBB,RES,BLC,MEA,SIT,PBQ,STJ,ALE,LRV,BOU,FRN,VIC,NEW,LOV,LER,VAL,HAD,ESK,MAB,DOU,BFE,CLF,OTT,WNG,VRE,THY,BEL,FUR,NGK,BDV,FRD,THL,SVS,KUV,UPN,UMQ,GDH,ATU,STF,SKT,FHB,NAQ,NRD,DMH,DNB,SCO,AMK,GIM,TAL,CNL,DAW,FCC,FMC,FSP,SMI,ISL,PIN,RAL,RAN,NAL,LYR,JAN,BJN,SOR,TRO,AND,RVK,DOB,HRN,KEV,MAS,KIL,IVA,ABK,MUO,KIR,SOD,PEL,OUJ,HAN,NUR,UPS,TAR,BRW,KAV,ARC,BET,FYU,EAG,CMO,GAK,PKR,CCS,TIK,AAE,ABG,AMS,API,ASP,BMT,BNG,BSL,CNB,CAN,CZT,DLR,DRV,EYR,GUA,GUI,HBK,HER,HLP,HON,HRB,IQA,IRT,ISK,KAK,KOU,MBO,MMB,NCK,PAF,PHU,PPT,SBA,SJG,SPT,SUA,TAM,TAN,TUC,VSS,NVS,LVV,PPI,MUT,LRM,KAT,KTN,CHD,MGD,MSR,ONW,KAG,CBI,WEW,WEP,EWA,MCQ,PBK,AIA,ASC,CSY,CTA,GLN,HTY,KDU,KNY,MAW,PST,TSU,HUA,TRW,AQU,LMM,LZH,QSB,TND,EBR,TEO,LEM,RIK,FIT,PUT,SER,CER,VLD,OSO,PNT,PAC,MCM,SPA,ELT,GZH,MLT,NOK,B11,B12,B14,B15,B17,B18,B19,B20,B21,B22,B23,B03,B04,HOR,PET,CUL,HOB

The Solar and Heliospheric Observatory (SOHO) Project Scientist Team. (2018). [database]. Retrieved from https://sohoftp.nascom.nasa.gov/sdb/goes/ace/daily/20031029_ace_mag_1m.txt

Torta, J. M., Marsal, S., & Quintana, M. (2014). Assessing the hazard from geomagnetically induced currents to the entire high-voltage power network in spain. *Earth, Planets and Space*, *66*, 1-17.

Tóth, G., De Zeeuw, D. L., Gombosi, T. I., Manchester, W. B., Ridley, A. J., Sokolov, I. V., & Roussev, I. I. (2007). Sun-to-thermosphere simulation of the 28–30 october 2003 storm with the space weather modeling framework. *Space Weather*, *5*(6). Retrieved from https://agupubs.onlinelibrary.wiley.com/doi/abs/10.1029/2006SW000272 doi: https://doi.org/10.1029/2006SW000272

Viljanen, A. (1997). The relation between geomagnetic variations and their time derivatives and implications for estimation of induction risks. *Geophysical Research Letters*, *24*(6), 631-634. Retrieved from https://agupubs.onlinelibrary.wiley.com/doi/abs/10.1029/97GL00538 doi: https://doi.org/10.1029/97GL00538

Villante, U., & Regi, M. (2008). Solar flare effect preceding halloween storm (28 october 2003): Results of a worldwide analysis. *Journal of Geophysical Research: Space Physics*, *113*(A3). Retrieved from https://agupubs.onlinelibrary.wiley.com/

doi/abs/10.1029/2008JA013132 doi: https://doi.org/10.1029/2008JA013132

Waskom, M. L. (2021). seaborn: statistical data visualization. *Journal of Open Source Software*, *6*(60), 3021. Retrieved from https://doi.org/10.21105/joss.03021 doi: 10.21105/joss.03021

Webb, D. F., Cliver, E. W., Crooker, N. U., Cyr, O. C. S., & Thompson, B. J. (2000). Relationship of halo coronal mass ejections, magnetic clouds, and magnetic storms. *Journal of Geophysical Research*, *105*, 7491-7508.

Wes McKinney. (2010). Data Structures for Statistical Computing in Python. In Stéfan van der Walt & Jarrod Millman (Eds.), *Proceedings of the 9th Python in Science Conference* (p. 56 - 61). doi: 10.25080/Majora-92bf1922-00a

Woodroffe, J. R., Morley, S. K., Jordanova, V. K., Henderson, M. G., Cowee, M. M., & Gjerloev, J. G. (2016). The latitudinal variation of geoelectromagnetic disturbances during large (dst < -100 nt) geomagnetic storms. *Space Weather*, *14*(9), 668-681. Retrieved from https://agupubs.onlinelibrary.wiley.com/doi/abs/10.1002/2016SW001376 doi: https://doi.org/10.1002/2016SW001376

World Data Center for Geomagnetism, Kyoto. (2018). [database]. Retrieved from https://wdc.kugi.kyoto-u.ac.jp/aeasy/index.html

Xu, Z., Gannon, J. L., & Rigler, E. J. (2013). Report of geomagnetic pulsation indices for space weather applications..

Investigating the Space Weather Impact of the 2003 Halloween Geomagnetic Storm by the Ground Magnetic Field Variations: a Global View

Hongyi Hu[1]

[1]The Overlake School

Abstract

Space weather is the phenomenon of solar storms and other events in space that can have impacts on Earth. They are a major concern for power grids which can be severely damaged by geomagnetic field variations during such natural phenomena. To reduce such impact and the possible consequences following, the study aims to determine how the storm's impact spreads across the Earth during a strong event, the October 29th, 2003 Halloween Storm. The impact of the Halloween Storm is analyzed by using global maps of geomagnetic variations to find where it is received and how it propagated. Cross-correlation is done on specific latitudinal and longitudinal distributed chains. The maps show that impacts are received first in high-latitude regions and then propagate toward mid- and low-latitude regions. The regions of impact during the first storm are on the magnetic dayside while the second storm is on the magnetic night side. The cross-correlation study shows that localized patterns occur more in the high-latitude regions with more intensive impacts, such as Norway, Finland, Sweden, Russia, and Canada. Global patterns occur more in the mid and equatorial regions with less intensive impacts. The mid-latitude countries such as France, UK, and the US can also be impacted during extreme events. The visualization package is developed and available to researchers and the industry. The global view of space weather impacts can help us to understand and mitigate the hazardous impacts on modern society.

Plain Language Summary

Space weather is the phenomenon of solar storms and other events in space that can have impacts on Earth. They are a major concern for power grids which can be severely damaged during such natural phenomena. To reduce the impact and the possible consequences, the study aims to determine how the storm's impact spreads across the Earth during a strong event: the October 29th, 2003 Halloween Storm. The impact of this storm is analyzed using a global map of geomagnetic variations to find the progression. Cross-correlation is applied to distinguish the global and localized features of impacts. The maps show that impacts are received first in high-latitude regions and then propagate toward lower latitude regions. The cross-correlation study shows that localized patterns occur more in the high-latitude regions with more intensive impacts, such as Norway, Finland, Sweden, and Canada. Global patterns occur more in the mid and equatorial regions with less intensive impacts. The mid-latitude countries such as France, UK, US can also be impacted during extreme events. The visualization package is developed and available to researchers and the industry. The global view of space weather impacts can help us to understand and mitigate the hazardous impacts on modern society.

1 Introduction

Space weather is the phenomenon of solar storms and other events in space that can have an impact on Earth. The main source of space weather is the Sun, which can produce solar flares (Hood & Priest, 1979; Kusano et al., 2004, 2012; Shibata & Magara, 2011), coronal mass ejections (CMEs) (Mcallister et al., 1996; Forbes, 2000; Webb et al., 2000; Hathaway & Wilson, 2006), and high-speed solar wind streams that cause significant impacts on modern society (Eastwood et al., 2017), affecting technologies such as radio communication, GPS and GNSS systems, and satellite communications, high-latitude aviation, Mining operations, power grids, and natural gas pipelines (Baker et al., 2008; Berger et al., 2020) . The results can disrupt radio communications, endanger astronauts, cause errors in GPS and GNSS systems, lose satellite communications, expose pilots and passengers to higher levels of radiation in high-latitude aviation, overload power grids, and accelerate corrosion of natural gas pipelines (Osella et al., 1998). As a result, space weather has significant implications for national security due to the capability to damage critical infrastructures, such as the electric grid. The US has a large space-based infrastructure and is almost exclusively reliant on an aging and stressed power grid, making it vulnerable to the effects of space weather. To mitigate these effects, the US has established a Federal Operating Concept for Impending Space Weather Events (FEMA Homeland Security, 2019), which focuses on operational and crisis planning. Space weather study has become one of the most important research in recent years.

Geostorms result in anomalies and disruptions to modern conveniences such as electrical power distribution networks. Space weather conditions on the ground generally originate from the interaction of the solar wind with the magnetosphere, which propagates down to the ionosphere and ground via magnetic field lines (Shiokawa, 2023). Geomagnetically induced currents (GICs) are set up by a geoelectric field (E) which arises from time variations in magnetic field B caused by ionospheric and magnetospheric currents and the conductive properties of the ground. The GICs can cause severe damages of power grids. Extreme space weather events are now recognized as a serious threat to worldwide technological infrastructure, e.g., (Boteler et al., 1998; Viljanen, 1997; Pulkkinen et al., 2017). For example, during the 1989 storm (D. H. Boteler, 2019), the entire grid was out of service within 90 seconds. The collapsed power grid left six million people and the rest of Quebec without electricity for nine hours in most places, and days in others. This geomagnetic storm caused about \$10 million dollars in damage to Quebec and tens of millions customers out of services. Extreme B field variations during the storm can be generated with a variety of spatial scales. They can occur in the auroral zone with fine spatial scales ($<\sim$100 km) or be excited by CMEs (Srivastava & Venkatakrishnan, 2002) and interplanetary shocks with global scales (Ngwira et al., 2013, 2015; Belakhovsky et al., 2018, 2019; Engebretson et al., 2019). Magnetometers have proven essential in this area for both research and real-time monitoring of B that drives GIC. Forecasting large GIC remains challenging as the largest GIC is not always concurrent with the largest geomagnetic depressions (Dimmock et al., 2019; Tóth et al., 2007) or elevated geomagnetic activity levels (Engebretson et al., 2020). So, it is important to use magnetometer observation to investigate the physics mechanism behind GICs and to verify the model predictions with observations (Kotzé et al., 2015). Since the 2003 Halloween Storm is the most intense storm in recent three decades, It has been studied by many researchers with different focus, such as the geomagnetic disturbance at lowest latitudes in the dayside hemisphere (Villante & Regi, 2008; Barbosa et al., 2015), the equatorial anomaly in the Brazilian sector(Batista et al., 2006), impacts on power grids at mid-latitudes(Schultz, 2012), geoelectric hazard maps for the Mid-Atlantic United States(Love et al., 2018), GICs on power network in New Zealand (Marshall et al., 2012), in Brazil (Barbosa et al., 2015), in Spain (Torta et al., 2014), in Great Britain (Orr et al., 2021), in Scotland (Simpson & Bahr, 2020), and in Japan(Ebihara et al., 2021). An insightful collection of research articles is listed in (Knipp, 2015) and a Geophysical Monograph on GICs and their impacts on power systems is published by (Gannon, 2019).

In this research paper, the impact of the Halloween Storm is analyzed by using global maps of geomagnetic variations to find where it is received and how it propagated. There are magnetic field data from 205 magnetometer observatories available for the 2003 Halloween Storm, which makes it possible to look at the global picture of the storm's impacts on magnetic field variations. The map is generated with Kriging interpolation and cross-correlation is done on specific latitudinal distribution chains and longitudinal distribution chains. The maps show that impacts are received first in high-latitude regions and then propagate toward mid- and low-latitude regions. Examining magnetic field variations caused by this great storm at a global scale allows for a better understanding of the questions: How did the 2003 Halloween storm impact the regions of the Earth from the point of view of magnetic field variations? What is the correlation between the magnitude of impact between the different latitude and longitude regions? How do different regions of the Earth are impacted differently? The answers to these questions will provide observational information during a solar storm to power grid operations and other crucial infrastructures (*National Space Weather Strategy and Action Plan*, 2019). It will help them to mitigate potential hazards caused by space weather. Also, by comparing the predicted value of geomagnetic field variations to global maps, space weather researchers will be able to assess the prediction's accuracy and how the model can be improved to achieve better and more accurate results.

In this research paper, the methodology and data used are presented in section 2; the results of global maps of magnetic field variations, and latitude and longitude difference of magnetic field variations during the storms are presented in section 3; discussion and a summary of these results are concluded in section 4.

2 Data and Methodology

For this research, the 2003 Halloween Storm was picked as it is the strongest solar storm in the last three decades that impacted the Earth since one in 1989. The Halloween storm lasted three days and had several waves of storms. Only the first two storms on October 29th, 2003 were selected due to the limited scale of research and data available on solar wind conditions. Storm-1 is defined as the period between 06-09 UT based on the level of Interplanetary Magnetic Field (IMF) based on observations from ACE Satellite and Sym-H index shown in Figure 1. Storm-2 is defined as 17-24UT.

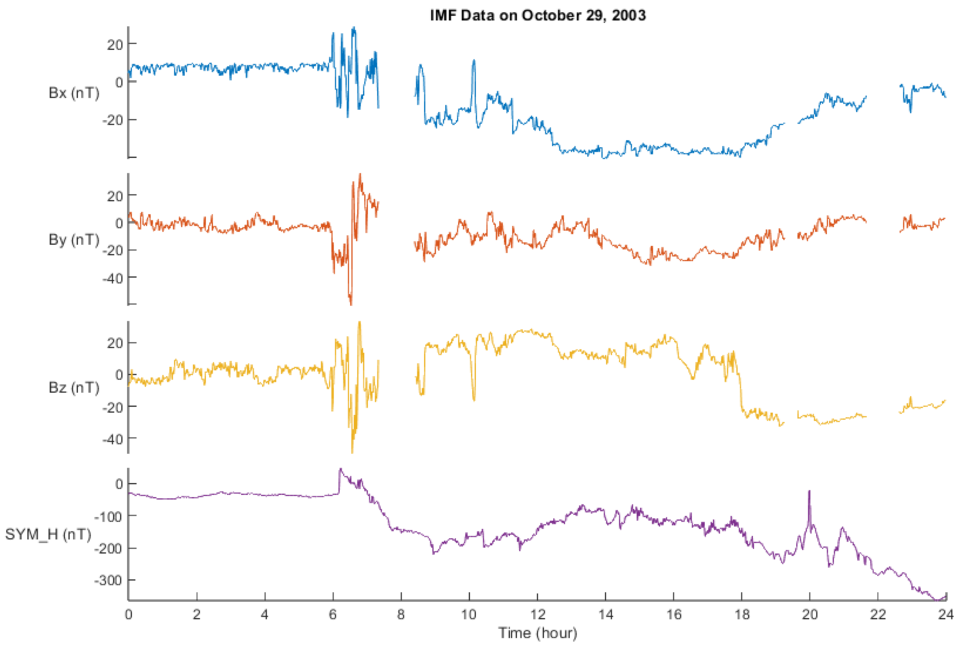

Figure 1: The missing data from the stacked plot is a result of extremely intense storms

There are two parts to the analysis. The first part was to develop global maps of magnetic variations during the Halloween Storm. The global map of magnetic field variations during the two storms was generated with MATLAB. The mesh grid was created with a precision of 1°. The base map loaded is the "landareas.shp" from the Mapping Toolbox™ in Matlab. The data points of the stations are then interpolated with Kriging interpolation (Xu et al., 2013) to generate a map, which is then overlaid on the base world map as "colormap" with the Matlab function mapshow(). The map is in the Projected Coordinate System so the geo coordinates match the Cartesian coordinates. Although the interpolation relies on Cartesian coordinates rather than geocoordinates, which means data points near the poles are skewed, this limitation is not significant enough for the purpose of this study. The accuracy of interpolation by kriging will also be limited as the number of stations is spatially sparse (Buck et al., 2002; Stoica & Moses, 2005).

After generating all the frames of global maps during the time interval, a Graphics Interchange Format (GIF) with all the frames was synthesized with PIL and glob modules in Python to easier observe the trend more over time. The frames and the GIF were used to predict the impact of the storm on modern society globally and its direction of spread by examining the geomagnetic impact on the map in chronological order. The second part is to perform a cross-correlation study between different regions on the Earth to find the different impacts between them.

Cross-correlation measures the similarity between two sets of time series data. It is used to determine how well two sets of data match up with each other by tracking the similarities (correlation coefficients) and the lag over time between each other. The possible range for the correlation coefficient is from 0 to +1.0. It can also determine the time lags between the sets of data.

The true cross-correlation sequence of two jointly stationary random processes, x_n and y_n, is given by

$$R_{xy}(m) = E\{x_{n+m}y_n^*\} = E\{x_n y_{n-m}^*\} \tag{1}$$

where $-\infty < n < \infty$, the $*$ denotes complex conjugation, and E is the expected value operator. The correlations with no normalization are

$$\hat{R}_{xy}(m) = \begin{cases} \sum_{n=0}^{N-m-1} x_{n+m}y_n^* & m >= 0 \\ \hat{R}_{xy}(-m) & m < 0 \end{cases} \tag{2}$$

and the output can then be normalized with

$$\hat{R}_{xy,coeff}(m) = \frac{1}{\sqrt{\hat{R}_{xx}(0)\hat{R}_{yy}(0)}}\hat{R}_{xy}(m) \tag{3}$$

To analyze how the longitude affects the two storms (Storm-1 and Storm-2), a few chains of stations are selected to run cross-correlation. In each chain, the stations are evenly distributed around the globe with varying magnetic local times (MLT) but a similar magnetic latitude. As the physics mechanisms behind this study are dependent on the magnetic field rather than geography, magnetic coordinates are used instead of geographical coordinates. The latitudes chosen are high-north, mid-north, equator, and south. Therefore a total of four chains for each storm is chosen. After stack plotting these stations with plot() function in Matlab, it was observed that the most significant feature of Storm-1 was between the period 05:59-07:39 UT on October 29th and that of Storm-2 between 17:24 21:34 UT. Any missing data in the series are linearly interpolated with R.

To analyze how the latitude affects the two storms, two chains for each storm were picked with varying latitudes and similar longitude. For Storm-1, one chain is before noon of MLT and the other is right after. The two chains of Storm-2 are before and after midnight of MLT. The stations chosen for Storm-1 is mostly identical to those for Storm-2 as the two storms are almost twelve hours apart. The difference between the two sets of stations chosen comes from the lack of available data for some of the stations in the other storm. For example, station AAE was chosen for the pr-midnight chain but not for the prenoon chain, and ELT was chosen for the prenoon chain but not for the pre-midnight chain.

For each chain, the series of data from the stations are cross-correlated with xcorr() function in Matlab and then stored the max correlation coefficients and the lags. Using this correlation and lag, two matrix colormaps for each chain were generated using pandas, seaborn and matplotlib modules in Python. A colormap is a matrix of values that define the colors for graphics objects such as surface, image, and patch objects. The colormap is drawn by mapping data values to colors in the colormap. By speculating the matrix colormaps, the local and global patterns of magnetic field variations at different stations can be revealed.

Data with a time resolution of one minute and a time interval from 00:00 UT, October 29, 2003 to 23:59 UT, October 29, 2003 was downloaded from SuperMAG (`supermag.jhuapl.edu`). Stations that contain more than 20 missing data points at the beginning or end of each of the two time periods (05:09 - 09:09 UTC, Oct. 29, 2003, and 17:24 UT, Oct. 29, 2003 - 00:24 UT, Oct. 30, 2003) were removed due to the inaccurate interpolation results of linear interpolation with an open end. That is when only one end of the period in interpolation was defined. This leaves 193 quality stations for the first period and 188 for the second. Solar wind data are from ACE satellites in the NASA database (https://sohoftp.nascom.nasa.gov/sdb/goes/ace/daily/). The temporal resolution of data is 60 seconds. The Interplanetary Magnetic Field (IMF) data are split into three components in Geocentric Solar Magnetospheric (GSM) coordinate (Maus & Lühr, 2005).

All datasets used in the study were open-source/publicly available. Data generated by this research project can be accessed at (`https://github.com/PythonOrC/SpaceWeather`)

3 Results

3.1 global maps of magnetic field variations

For the series of storms that happened during the three days of the 2003 Halloween Storm, the first two storms were selected for this research project. Storm-1 is defined as the period between 06-09 UT based on the level of satellite-based Interplanetary Magnetic Field (IMF) and ground-based magnetic field measurements. Storm-2 is defined as 17-24UT.

Most of the activities and variations in Storm-1 were on the dayside around noon (MLT). At 05:59 UT, the value of IMF Bz first turned negative, meaning that reconnection will happen soon. At 06:13 UT [as shown in Fig 2(a), the impact of the negative IMF Bz in 05:59 UT showed up on the dayside near Finland, Norway, and Sweden with a Bn of -1000 nT. The time lag between IMF Bz turning southward (negative) and the impact on the ground magnetic field is 14 minutes, which is shorter than the statistical value of 20-25 minutes (Akasofu, 2007) due to the strong and fast CME impacts. At 06:20 UT [as shown in Fig 2(b), the dBn value was low as -2000nT in high-latitude regions on both hemispheres of the Earth (near Finland and Norway in the northern hemisphere and near station B15 in the southern hemisphere). This shows an enhancement of the storm. Then, at 06:49 UT [as shown in Fig 2(c)], the region of impact enlarged from the two local regions to all high-latitude regions and expanded toward mid-latitude regions in both hemispheres (near Germany, Denmark, Poland, and the northern UK in the northern hemisphere and near the South Atlantic Ocean and B04 in the Southern Hemisphere). The strongest dBn is less than -2800nT and more than 1500nT and presents an oval shape. At 07:02 UT[as shown in Fig 2(d)], the region of impact expanded to France and north of Spain with an intensity of about -800 nT in the northern hemisphere, South Africa (-900 nT), and Australia (-500 nT) in the southern hemisphere. Finally, at 08:05 UT [as shown in Fig 2(e)], the regions recovered from the storm impact with minor negative dBn variations globally in mid and high latitudes.

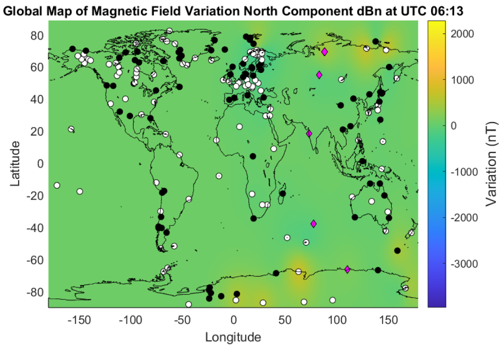

(a) UTC 06:13

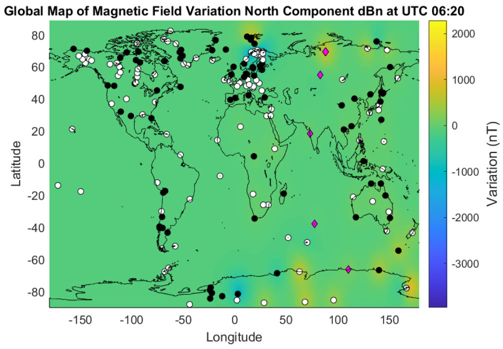

(b) UTC 06:20

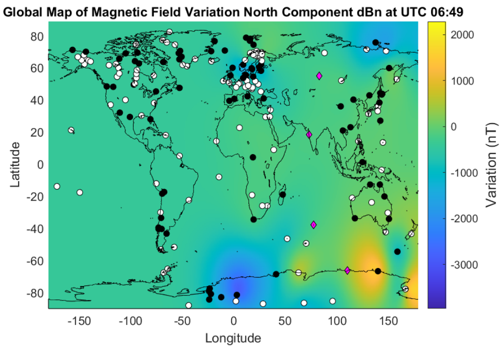

(c) UTC 06:49

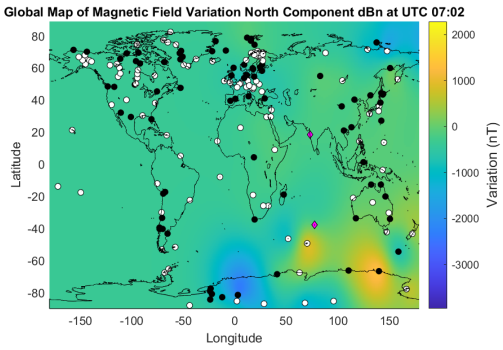

(d) UTC 07:02

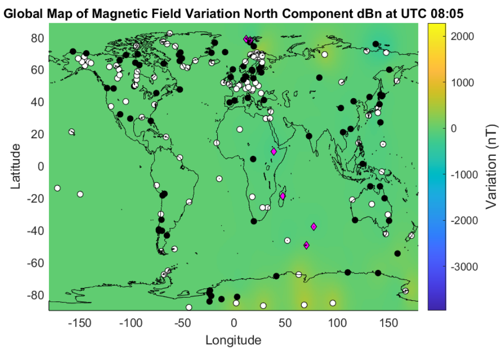

(e) UTC 08:05

Figure 2: Key frames in the progression of Storm 1. Yellow represents positive variation and blue represents negative variation, the black and white markers alternate every 10 degrees in terms of magnetic latitude. The purple markers represent the MLT noon.

For Storm-2, the main regions of impact are around Midnight MLT with several substorms happening one after another. The regions of impact were mostly near Finland, Norway, and Sweden. At 17:33 UT, a negative variation appeared on both sides of the pole with Svalbard reaching -700nT in the North and B04 Reaching -500nT in the South [as shown in Fig 3(a)]. Between 17:33 UT and 18:20 UT, there is a small substorm happening in both hemispheres with multiple positive-negative pairs observed. This indicates that there is a reconnection happening. At 18:20 UT, the storm started fading although IMF Bz is still

-20 nT[as shown in Fig 3(b)]. There are no significant changes even until 18:55 UT, which is when a new substorm happened [as shown in Fig 3(c)]. At 19:15 UT the variation intensity increased in Russia and Australia also rose in variation at 19:38 [as shown in Fig 3(d) and Fig 3(e)]. At 19:49 UT, this storm reached its peak impacts. Expanding to Danmark, the majority of Russia with max intensity of -2500 nT at KTN in the northern hemisphere, and south of New Zealand, South Indian Ocean, and South Pacific Ocean with the max impact of -2500 nT at MCQ in the southern hemisphere [as shown in Fig 3(f)]. The variations eased at 21:00 UT and another smaller substorm happened between 21:03 and 22:29 UT impacting Finland, Norway, and Sweden [as shown in Fig 3(g)].

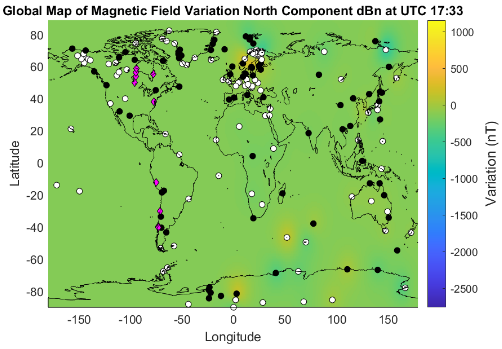

(a) UTC 17:33

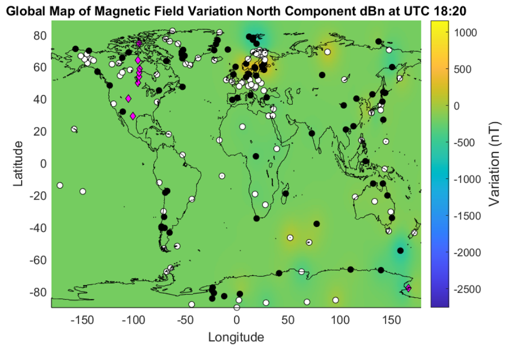

(b) UTC 18:20

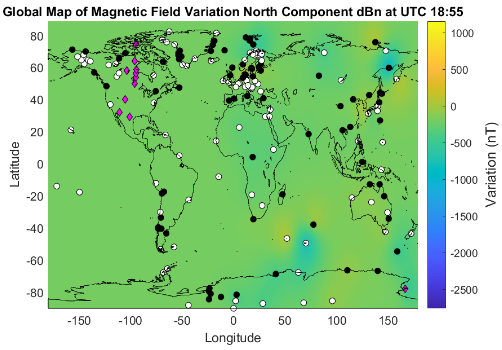

(c) UTC 18:55

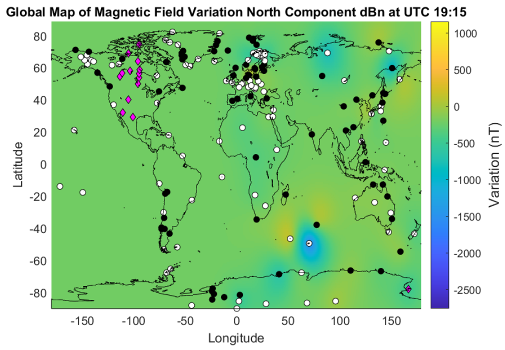

(d) UTC 19:15

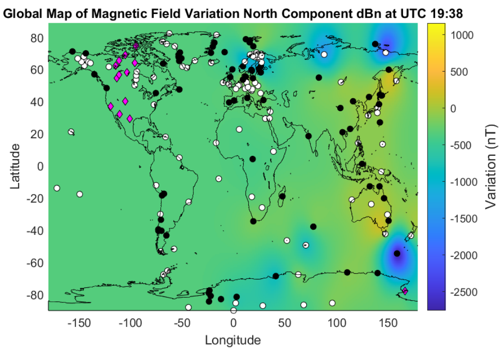

(e) UTC 19:38

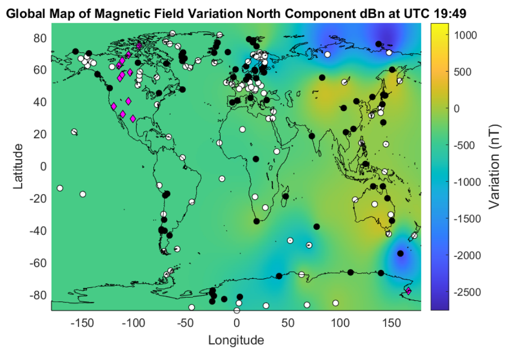

(f) UTC 19:49

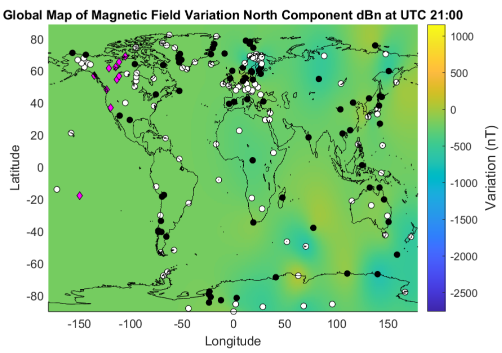

(g) UTC 21:00

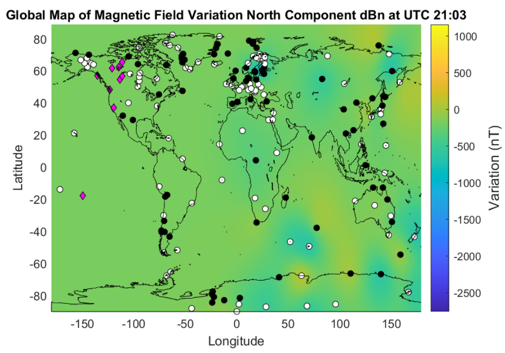

(h) UTC 21:03

Figure 3: Key frames in the progression of Storm 2. Same label setting as Fig 2

3.2 Cross-Correlation Study

By observing the colormaps of the cross-correlation for Storm-1 at pre-noon and afternoon MLT chains [as shown in Fig 4], it can be concluded that local signatures dominate high-latitude regions in both the northern and southern hemispheres shown by low correlation coefficients and large lags, such as ALE (MagLat 87.2°), HRN (MagLat 74.2°), BJN (MagLat 71.5°), MAW (MagLat -70.3°) in pre-noon chain and CHD (MagLat 65.1°), MGD (MagLat 53.9°), LEM(MagLat -53.2°), DRV (MagLat -80.5°) in afternoon chain. For mid- and low-latitude regions, from TAR (MagLat 54.5°) to CZT (MagLat -53.2°) in pre-noon chain and from MSR (MagLat 53.9°) to KDU (MagLat -21.8°) in the afternoon chain, the correlation coefficients between these stations are high and the lags between them are low, which indicates that there is a clear global signature between all of them. The maximum and minimum dBn value listed in Table 1 for prenoon chain and Table 2 for afternoon. It shows that the most intense variations occurring at 55°-70°MagLat regions for prenoon chain. For afternoon chain, only CHD and DRV shows strong disturbances of over 2000 nT while the rest of stations varying at a range of 200 nT. Overall, more local signatures dominate above 55°whereas the global signatures dominate stations below 55°.

IAGA	**MAGLON**	**MAG LAT**	**MLT**	**Min dBn**	**Max dBn**
MAW	90.3	−70.3	6.7	− 540.8	967.2
CZT	106.2	−53.2	7.8	− 814.6	2.9
LMM	100.1	−35.9	7.4	− 424.8	41.2
ELT	106.6	22.7	7.8	− 424.0	23.1
QSB	107.4	27.8	7.8	− 623.2	12.3
ISK	101.5	35.6	7.4	− 566.4	− 21.4
SUA	99.5	40.4	7.3	− 722.9	8.0
LVV	98.1	45.5	7.2	− 729.7	− 16.7
HLP	95.0	50.8	7.0	− 837.7	− 17.6
TAR	102.8	54.5	7.5	−1133.5	29.1
HAN	104.4	58.7	7.6	−1422.8	412.1
OUJ	106.0	61.0	7.7	−1598.1	914.3
SOD	107.1	64.0	7.8	−1771.3	617.3
SOR	105.9	67.4	7.7	−2082.6	399.1
BJN	107.8	71.5	7.9	−1342.8	595.1
HRN	109.0	74.2	7.9	− 506.4	675.4
ALE	94.0	87.2	6.9	− 263.3	2286.8

Table 1: Prenoon Chain Stations Info

IAGA	MAGLON	MAGLAT	MLT	Min dBn	Max dBn
DRV	−124.1	−80.5	16.4	− 103.1	1885.3
LEM	−133.2	−53.2	15.8	− 86.6	83.1
ASP	−152.7	−34.0	14.5	− 61.7	105.1
KDU	−155.2	−21.8	14.3	− 108.8	55.1
WEP	−145.3	−21.4	15.0	− 118.3	57.9
WEW	−144.3	−11.6	15.1	− 137.2	67.1
GUA	−144.0	6.2	15.1	− 137.7	62.5
CBI	−146.4	20.0	14.9	− 130.0	44.5
KAG	−157.2	24.8	14.2	− 124.6	58.8
HTY	−148.5	26.2	14.8	− 176.7	43.9
KAK	−148.0	29.3	14.8	− 149.4	31.9
ONW	−146.8	31.6	14.9	− 141.5	31.0
RIK	−144.7	36.7	15.0	− 137.9	42.8
MSR	−146.0	37.7	14.9	− 133.7	74.2
MGD	−140.4	53.9	15.3	− 121.6	117.5
CHD	−146.9	65.1	14.9	−1681.8	807.9

Table 2: Afternoon Chain Stations Info

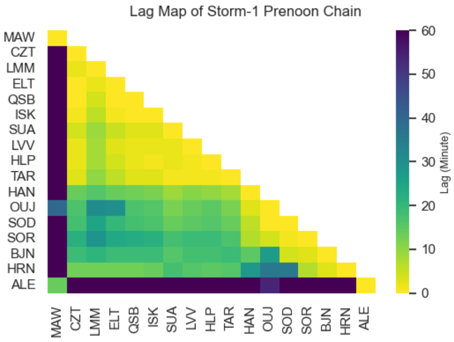

(a) Storm-1 prenoon chain lag

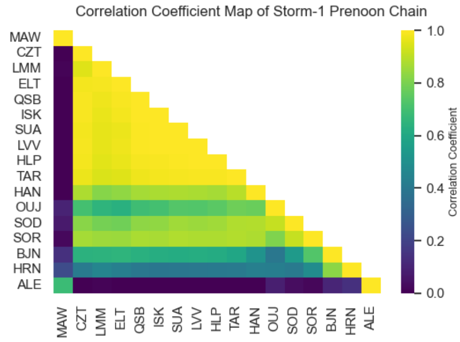

(b) Storm-1 prenoon chain correlation coefficient

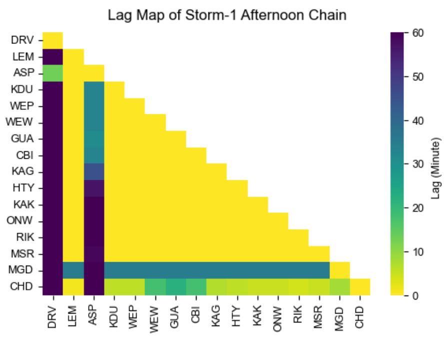

(c) Storm-1 afternoon chain lag

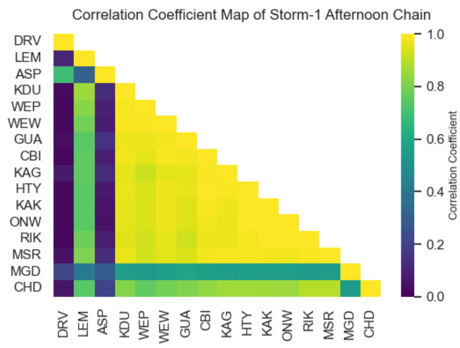

(d) Storm-1 afternoon chain correlation coefficient

Figure 4: Cross Correlation result of Storm-1 prenoon and afternoon chain

In order to investigate the details of how impacts change at different latitudes, four more chains are picked by stations at similar magnetic latitudes but longitudinally distributed as equally as possible around the globe. The four chains are at north-high latitude (near 60°), north-mid latitude (near 40°), equator, and south (below -50°). There is no south-mid latitude chain because of a lack of coverage at in the southern hemisphere. For Storm-1, at the north high-latitude chain [shown in Fig 5, there are localized features between stations that are located close to each other within 1-2 MLT hours. Small lags and high correlations are observed between stations BRW, KAV, ARC, FSP, CNL, BLC, and RAN, which are located from 17:47 to 23:02 MLT, suggesting that the variations occurring in these regions are by the same physics mechanism.

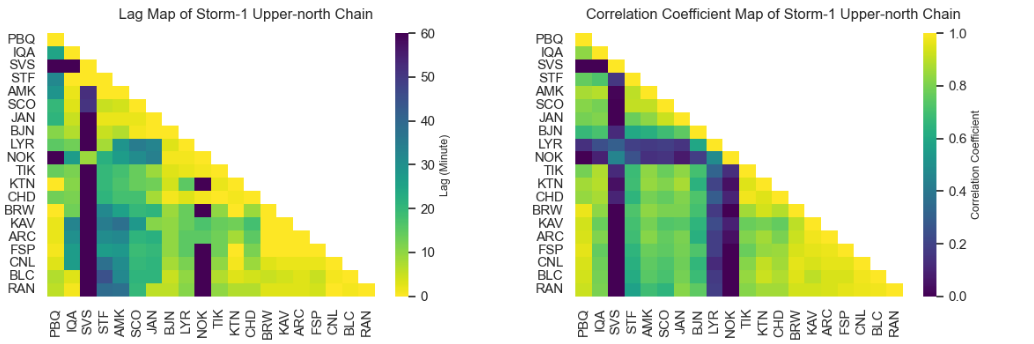

(a) Storm-1 north high-latitude chain lag

(b) Storm-1 north high-latitude chain correlation coefficient

Figure 5: Cross Correlation result of Storm-1 north high-latitude chain

In the north mid-latitude chain, the stations on the dayside (NVS, IRT, BMT, PPI, MSR, PET from 11:04 to 15:48 MLT) and night side (VIC, FRN, TUC, BOU, DLR, BSL from 20:26 to 23:23 MLT) are affected by different mechanism as the two sides show higher correlations and smaller lags amongst themselves but aren't related across sides [as shown in Fig 6].

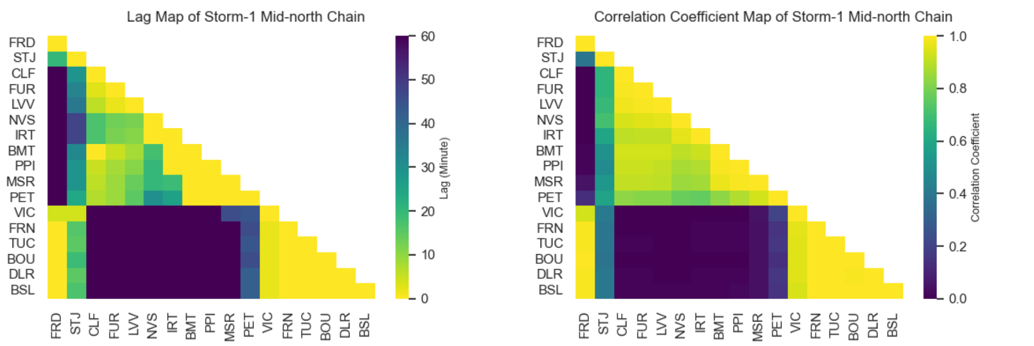

(a) Storm-1 north mid-latitude chain lag

(b) Storm-1 north mid-latitude chain correlation coefficient

Figure 6: Cross Correlation result of Storm-1 north mid-latitude chain

In the equator chain, the stations are similarly divided between dayside (MBO, TAM, BNG, MLT, AAE, ABG, PHU, TND, GUA from 04:32 to 15:04 MLT) and nightside (API, HON, PPT, HUA, VRE, KOU from to 18:11 to 02:24 MLT) with high correlation amongst each side but the two show little relationship with each other [as shown in Fig 7].

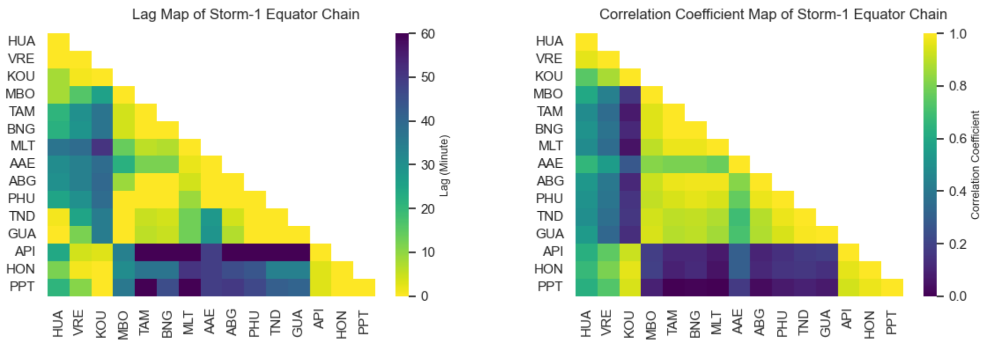

(a) Storm-1 equator chain lag (b) Storm-1 equator chain correlation coefficient

Figure 7: Cross Correlation result of Storm-1 equator chain

Stations from the south high-laitude chain are slightly different. Their correlations are small and lags are high between stations, except for the closely located stations of B03, B23, B14, B15, B04. This is probably due to the high magnitude of the variation [as shown in Fig 8].

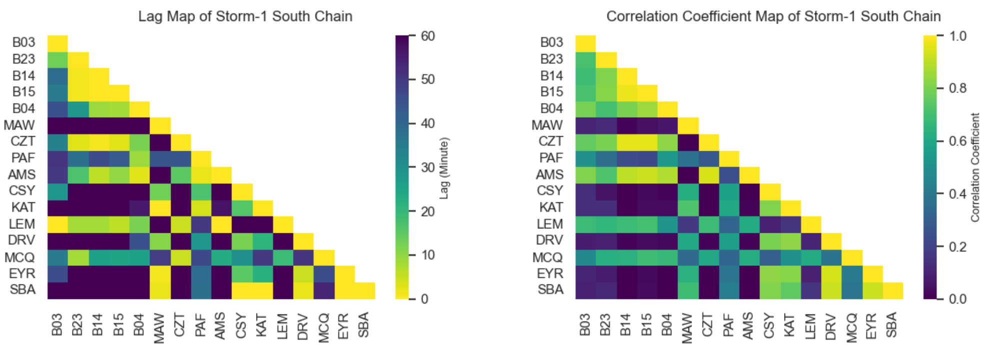

(a) Storm-1 south chain lag (b) Storm-1 south chain correlation coefficient

Figure 8: Cross Correlation result of Storm-1 south chain

For Storm-2, since it happened 12 hours after Storm-1, similar stations are selected as pre-midnight and after-midnight chains shown in Tables 3 and 4. The magnitudes of dBn variations are strong between 55°-75°for the pre-midnight chain, which peaked over 2000 nT at SOD (MagLat 64.0°). As a comparison, the variations of dBn at mid- and low-latitude stations are near 400-600 nT. For the after-midnight chain, the variations at high-latitude stations above 55°are over 1000-2000 nT, while variations at the mid- and low-latitude stations are around 200-300 nT.

As shown in Fig 9 (a) and (b), the colormaps of the lag and correlation at the pre-midnight chain present that variations at HBK, BNG, AAe, QSB, ISK, SUA, and LVV are similar to each other with high correlations and low lag. These stations are located between -36.0°and 40.4°in the mid- and low-latitudes. The correlations decrease at the stations located about 50°, especially for the stations at very high latitudes over 70°such as BJN, HRN, NRD, ALE, and MAW. For the after-midnight chain of Storm-2 present, the high correlation and low lag show global effects in mid- and low-latitude regions, while impacts at high-latitude regions (CHD at MagLat 65.1°, KTN at MagLat 70.4°, DRV at MagLat -80.5°) are the opposite. This could be attributed to the larger intensity of Field Aligned Currents (FACs) at high-latitude regions [as shown in Fig 9 c and d].

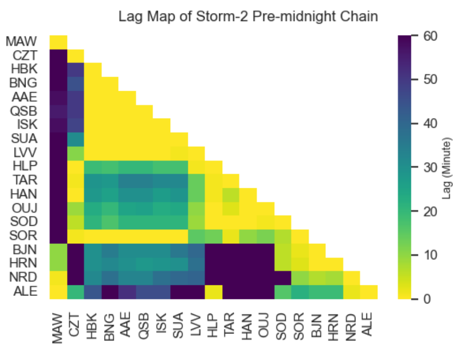

(a) Storm-2 pre-midnight chain lag

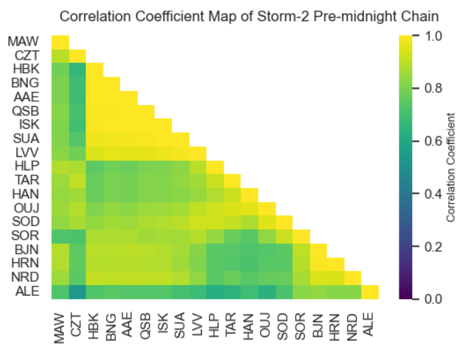

(b) Storm-2 pre-midnight chain correlation coefficient

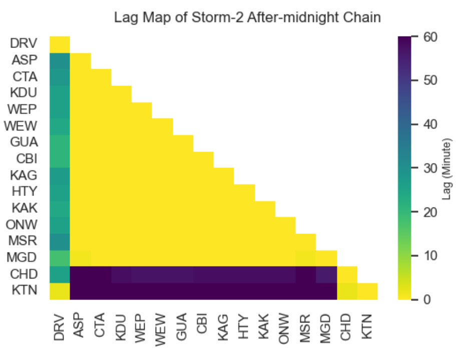

(c) Storm-2 after-midnight chain lag

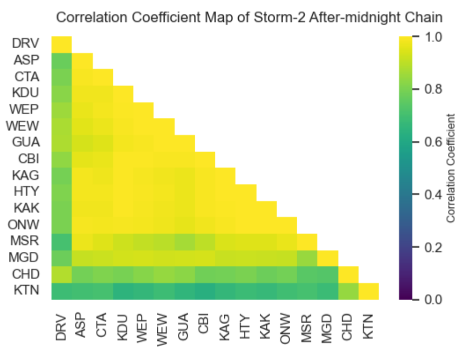

(d) Storm-2 after-midnight chain correlation coefficient

Figure 9: Cross Correlation result of Storm-2 pre-midnight and after-midnight chain

IAGA	MAGLON	MAGLAT	MLT	Min dBn	Max dBn
MAW	90.3	−70.3	18.9	−1101.3	119.4
CZT	106.2	−53.2	19.9	−1093.9	206.0
HBK	95.3	−36.0	19.2	− 268.2	−106.3
BNG	90.3	− 7.8	18.9	− 402.3	−163.3
AAE	110.7	0.4	20.2	− 367.8	−146.8
QSB	107.4	27.8	20.0	− 357.3	−100.3
ISK	101.5	35.6	19.6	− 293.0	− 77.3
SUA	99.5	40.4	19.5	− 366.7	− 63.5
LVV	98.1	45.5	19.4	− 399.9	− 48.0
HLP	95.0	50.8	19.2	− 794.2	3.0
TAR	102.8	54.5	19.7	−1063.3	254.7
HAN	104.4	58.7	19.8	−1853.2	407.4
OUJ	106.0	61.0	19.9	−1918.1	394.8
SOD	107.1	64.0	20.0	−2035.4	138.4
SOR	105.9	67.4	19.9	−1346.9	3.7
BJN	107.8	71.5	20.0	−1133.9	29.3
HRN	109.0	74.2	20.1	−1046.9	3.6
NRD	103.2	81.1	19.7	− 446.3	92.3
ALE	94.0	87.2	19.1	−1056.9	377.9

Table 3: Pre−midnight Chain Stations Info

IAGA	MAGLON	MAGLAT	MLT	Min dBn	Max dBn
DRV	−124.1	−80.5	4.6	− 953.1	−132.3
ASP	−152.7	−34.0	2.7	− 182.1	57.0
CTA	−139.6	−29.1	3.6	− 209.5	20.1
KDU	−155.2	−21.8	2.5	− 195.4	2.9
WEP	−145.3	−21.4	3.2	− 231.9	− 28.5
WEW	−144.3	−11.6	3.2	− 250.6	− 51.2
GUA	−144.0	6.2	3.3	− 274.3	− 86.8
CBI	−146.4	20.0	3.1	− 218.6	− 33.8
KAG	−157.2	24.8	2.4	− 154.8	30.3
HTY	−148.5	26.2	3.0	− 245.8	24.6
KAK	−148.0	29.4	3.0	− 213.4	20.0
ONW	−146.8	31.6	3.1	− 212.5	28.3
MSR	−146.0	37.7	3.1	− 219.1	117.6
MGD	−140.4	53.9	3.5	−1230.4	− 9.9
CHD	−146.9	65.1	3.1	−2222.7	− 96.3
KTN	−158.2	70.4	2.3	−2507.5	267.7

Table 4: After-midnight Chain Stations Info

In the north high-latitude chain, generally the correlations are high and lags are low for most stations except for ARC, KAV, KTN, NOK. It should be noted that there are very strong impacts at ARC, KAV, KTN, NOK of about 1000 2000 nT, which could be a cause of this deviation [as shown in Fig 10].

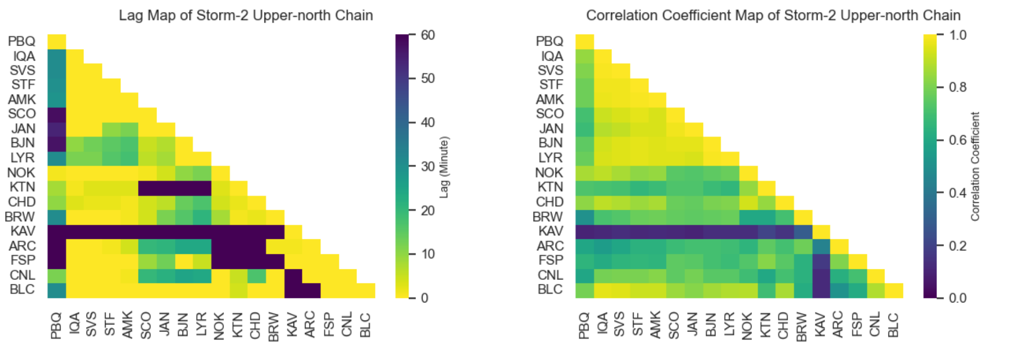

(a) Storm-2 north high-latitude chain lag

(b) Storm-2 north high-latitude chain correlation coefficient

Figure 10: Cross Correlation result of Storm-2 north high-latitude chain

In the north mid-latitude chain, the stations on the dayside (FRD, DLR, BOU, TUC, FRN, VIC) show higher correlations and smaller lags amongst each other; while the stations on the night side (NVS, IRT, BMT, PPI, MSR, PET) also have similar features [as shown in Fig 11].

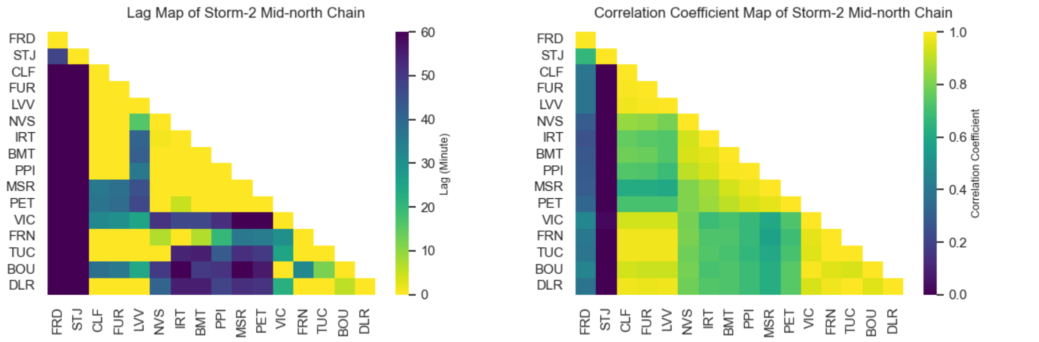

(a) Storm-2 north mid-latitude chain lag

(b) Storm-2 north mid-latitude chain correlation coefficient

Figure 11: Cross Correlation result of Storm-2 north mid-latitude chain

The stations from the equator chain have high correlations and the lags are 0, which shows that there is a global impact at the equator regions. This is due to the small impacts of Storm-2 at the equator regions, with variation only reaching 100 nT [as shown in Fig 12].

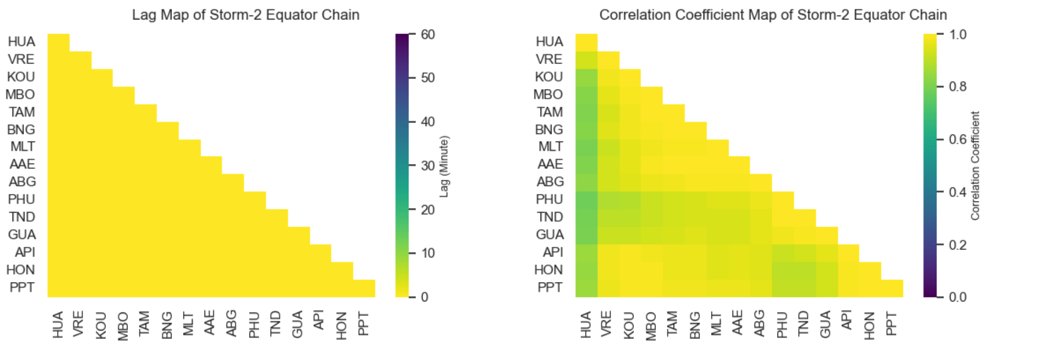

(a) Storm-2 equator chain lag

(b) Storm-2 equator chain correlation coefficient

Figure 12: Cross Correlation result of Storm-2 equator chain

The stations in the south chain present little correlation and high lags except for the closely located stations of B23, B14, B15, B04. This suggests that the variations these stations recorded have different drivers [as shown in Fig 13].

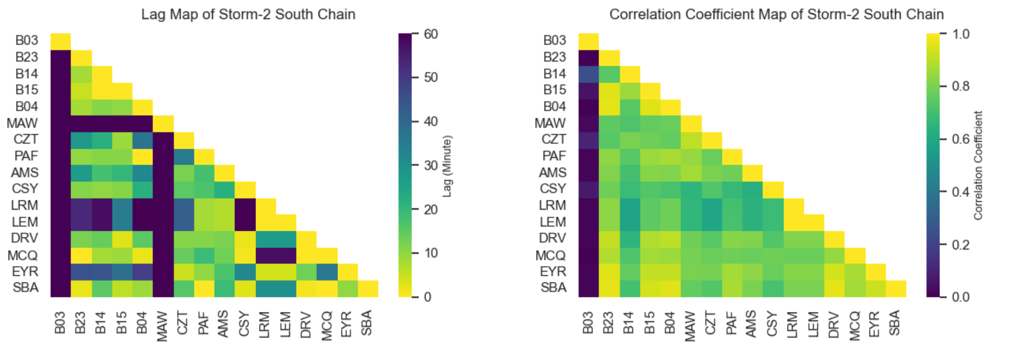

(a) Storm-2 south chain lag

(b) Storm-2 south chain correlation coefficient

Figure 13: Cross Correlation result of Storm-2 south chain

4 Discussion and Conclusion

The results of the global maps show that impacts at high latitudes occurred first for Storm-1 and 2 on 29 October 2003 Halloween Storm. Then, the regions of impact expanded from high-latitude to mid- and low latitudes. Aurorae were observed at mid- and low-latitudes as far south as Texas and the Mediterranean countries of Europe. The first impact located at high-latitude regions can be explained by the southward IMF (shown in Fig 1) leading to magnetic field reconnection and energy and particles are transported to polar regions first (Kamide, 2006) (Tóth et al., 2007). The physics mechanism of magnetic field variations can be explained by current systems associated with the growth, expansion, and recovery phases of substorms (Akasofu, 2007).

The results of the global maps show that high latitudes between 55°and 75°are the most intense regions of impact for Storm-1 and 2. The dBn value was as low as -2800nT near B15 (MagLong 36.7°, MagLat -68.6°) in high-latitude regions for Storm-1. For Storm-2, it is -2500 nT near MCQ (MagLong -111.74, MagLat -64.39). As one of the regions of impacts shown by the global maps, the Sydkraft utility group in Sweden reported that strong GICs over Northern Europe caused transformer problems and even a system failure and subsequent blackout. During the expansion to mid- and low-latitude periods, the north of Spain experienced an intensity of impact of about -800 nT in the northern hemisphere, and South Africa experienced -900 nT of impact in the southern hemisphere. Twelve transformers in South Africa were disabled and had to be replaced. These results matched the previous study carried by (Woodroffe et al., 2016), in which it shows that the most intensive impacts are located at high magnetic latitude regions. The variations of magnetic field vary from 700 nT at 45-50 degree of magnetic latitude to 2800 nT at 60-65 degree.

The cross-correlation results show that localized patterns occur more in the high-latitude regions and the regions of more intensive impacts, such as the pre-noon chain in Storm-1, pre-midnight chain in Storm-2, and high-latitude chains in both Storms, because the dynamics of energy and particle inputs are associated with localized field-aligned currents (FACs) at these regions. The global patterns occur more in the mid and equatorial regions and these regions show less intensive impacts, such as the afternoon chain in Storm-1, after-midnight chain in Storm-2, and equatorial chains in both storms, because the impacts from large-scale variations of currents (ring currents, magnetopause currents) are not as strong as localized FACs and other features near ground.

Due to the data availability and coverage, the global maps and cross-correlation analysis of latitudinal and longitudinal chains can provide information over large spatial grids. The limitation of kriging interpolation depends on the distance between nodes. To provide better space weather information, it urges the development of better and more dense spatial and temporal coverage of magnetometer observations. To cover the fine localized dynamics of possible GIC impacts, 100 km by 100 km spatial coverage with 1-second temporal resolution will be ideal.

As the conclusion of research paper, the global map presents a big picture that shows where the impacts first occur on the Earth, how the regions of impact expanded, and how intense the impacts were. The regions with strong impacts, such as Sweden, and South Africa, had experienced power outages over hours. The global and local feature analysis carried out by cross-correlation study shows that the intensive impacts are associated with more dynamic and localized features. To provide better space weather impacts and to improve the understanding of space weather mechanisms, it urges the development of better magnetometers or other space weather observations in both spatial and temporal domains. The global view of space weather impacts can help us to understand and mitigate the hazardous impacts on modern society. The visualization package is developed and available on GITHUB. It could be used by the space weather community. The researchers who work on space weather predictions could use the codes to generate the maps of predicted geomagnetic field variations and compare them with the observed global maps of geomagnetic field variations, to verify whether the predictions match the observation and how to improve the model to get better and more accurate results.

In the future, with more spatial coverage of magnetometer observations, the global maps could show detailed regional impacts at 100 km by 100 km grid scales. Combining the maps with other GIS information databases could provide the space weather impact estimation not only on power grid operations, but also on other crucial infrastructures, including hospitals, financial centers, emergency response, and national security-related agencies. During the last decade, the US government has developed a series of government reports and national action plans (*National Space Weather Strategy and Action Plan*, 2019) on space weather operations with multiple agencies, including NSF, NASA, FEMA, National Science and Technology Council, National Security Council, Office of Science and Technology Policy, DoC, DoE, DoD, and others. The importance of space weather has been promoted to the national strategic level. The research on space weather impact will make more and more valuable contributions with the coming of the space era.

5 Open Research

The global map model, the correlation map model, the code used to generate these models, and the data used are all available at GitHub via `https://github.com/PythonOrC/SpaceWeather` with GNU General Public License v3.0. An archive of this can be found in this citation (Hu, 2023). Matlab (Inc., 2022) was used to generate the global map model frames, and the GIF was synthesized with Python and the Pillow module (Clark, 2015). The correlation map was generated with Python and the following modules: pandas(pandas development team, 2020; Wes McKinney, 2010), numpy(Harris et al., 2020), matplotlib(Hunter, 2007), seaborn(Waskom, 2021). The ground magnetometer data used in this research was provided by SuperMAG(Gjerloev, 2012; SuperMAG, 2009). The ACE data used in this study was provided by The Solar and Heliospheric Observatory (SOHO)(The Solar and Heliospheric Observatory (SOHO) Project Scientist Team, 2018). The SYM_H data used in this paper was provided by the WDC for Geomagnetism, Kyoto (`http://wdc.kugi.kyoto-u.ac.jp/wdc/Sec3.html`)(World Data Center for Geomagnetism, Kyoto, 2018; S et al., 2022).

Acknowledgments

For the ground magnetometer data, we gratefully acknowledge the SuperMAG (`https://supermag.jhuapl.edu/info/?page=acknowledgement`) and its collaborators: INTERMAG-

NET, Alan Thomson; CARISMA, PI Ian Mann; CANMOS, Geomagnetism Unit of the Geological Survey of Canada; The S-RAMP Database, PI K. Yumoto and Dr. K. Shiokawa; The SPIDR database; AARI, PI Oleg Troshichev; The MACCS program, PI M. Engebretson; GIMA; MEASURE, UCLA IGPP and Florida Institute of Technology; SAMBA, PI Eftyhia Zesta; 210 Chain, PI K. Yumoto; SAMNET, PI Farideh Honary; IMAGE, PI Liisa Juusola; Finnish Meteorological Institute, PI Liisa Juusola; Sodankylä Geophysical Observatory, PI Tero Raita; UiT the Arctic University of Norway, Tromsø Geophysical Observatory, PI Magnar G. Johnsen; GFZ German Research Centre For Geosciences, PI Jürgen Matzka; Institute of Geophysics, Polish Academy of Sciences, PI Anne Neska and Jan Reda; Polar Geophysical Institute, PI Alexander Yahnin and Yarolav Sakharov; Geological Survey of Sweden, PI Gerhard Schwarz; Swedish Institute of Space Physics, PI Masatoshi Yamauchi; AUTUMN, PI Martin Connors; DTU Space, Thom Edwards and PI Anna Willer; South Pole and McMurdo Magnetometer, PI's Louis J. Lanzarotti and Alan T. Weatherwax; ICESTAR; RAPIDMAG; British Artarctic Survey; McMac, PI Dr. Peter Chi; BGS, PI Dr. Susan Macmillan; Pushkov Institute of Terrestrial Magnetism, Ionosphere and Radio Wave Propagation (IZMIRAN); MFGI, PI B. Heilig; Institute of Geophysics, Polish Academy of Sciences, PI Anne Neska and Jan Reda; University of L'Aquila, PI M. Vellante; BCMT, V. Lesur and A. Chambodut; Data obtained in cooperation with Geoscience Australia, PI Andrew Lewis; AALPIP, co-PIs Bob Clauer, Michael Hartinger, and Zhonghua Xu; MagStar, PI Jennifer Gannon; SuperMAG, PI Jesper W. Gjerloev; Data obtained in cooperation with the Australian Bureau of Meteorology, PI Richard Marshall. For the solar wind and IMF data, we gratefully acknowledge NASA Solar and Heliospheric Observatory (SOHO) Project website (`https://sohoftp.nascom.nasa.gov/sdb/goes/ace/daily/`).

Appendix A Table of All Stations Used and Related Information

IAGA	GEOLON	GEOLAT	MAGLON	MAGLAT
AAE	38.77	9.03	110.68	0.42
ABG	72.87	18.62	145.39	12.09
ABK	18.82	68.35	101.53	65.31
AIA	295.74	-65.25	9.11	-50.28
ALE	297.5	82.5	94	87.16
AMK	322.37	65.6	53.63	69.05
AMS	77.57	-37.8	138.9	-49.14
AND	16.03	69.3	100.1	66.45
API	188.22	-13.8	-97.37	-15.58
AQU	13.32	42.38	87.29	36.34
ARC	214.44	68.12	-96.08	68.83
ASC	345.62	-7.95	56.11	-15.2
ASP	133.88	-23.77	-152.74	-34.04
ATU	306.43	67.93	38.14	74.2
B03	291.88	-67.57	7.64	-52.47
B04	41.08	-68.58	73.64	-66.18
B11	336.58	-77.51	30.11	-63.47
B12	335.88	-79.08	29.1	-64.7
B14	337.74	-80.89	28.8	-66.31
B15	2.97	-81.49	36.66	-68.6
B17	347.76	-82.9	30.3	-68.53
B18	336.14	-84.35	25.78	-69.17
B19	2.06	-85.36	29.96	-71.17
B20	95.98	-85.36	30.09	-77.75
B21	28.41	-87	28.91	-73.39
B22	68.17	-86.51	30.66	-75.54
B23	316.13	-88.03	19.78	-72.18
BDV	14.02	49.07	89.32	44.57
BEL	20.8	51.83	95.93	47.67
BET	208.45	66.9	-100	66.55
BFE	11.67	55.62	89.31	52.12
BJN	19.2	74.5	107.77	71.51
BLC	263.99	64.32	-31.98	73.76
BMT	116.2	40.3	-171	34.7
BNG	18.57	4.33	90.32	-7.75
BOU	254.76	40.14	-40.05	48.93
BRW	203.38	71.32	-108.13	70.21
BSL	270.36	30.35	-19.21	41.22
CAN	149.36	-35.31	-133.08	-45.32

IAGA	GEOLON	GEOLAT	MAGLON	MAGLAT
CBB	254.97	69.12	-50.3	77.08
CBI	142.3	27.15	-146.38	19.99
CCS	104.28	77.72	175.87	72.2
CER	289.4	-33.45	0.67	-20.22
CHD	147.89	70.62	-146.94	65.13
CLF	2.27	48.02	79.15	43.53
CMO	212.14	64.87	-95.41	65.14
CNB	150.7	-34.1	-131.84	-43.83
CNL	248.75	65.75	-56.62	73.05
CSY	110.53	-66.28	156.87	-80.78
CTA	146.3	-20.1	-139.56	-29.11
CUL	149.58	-30.28	-134.06	-39.82
CZT	51.87	-46.43	106.22	-53.2
DAW	220.89	64.05	-87.04	65.99
DLR	259.08	29.49	-33.4	38.82
DMH	341.37	76.77	85.13	77.2
DNB	339.78	74.3	78.89	75.06
DOB	9.11	62.07	90	59.29
DOU	4.6	50.1	81.65	46.03
DRV	140.01	-66.67	-124.11	-80.5
EAG	218.84	64.78	-89.46	66.32
EBR	0.49	40.82	76.07	33.86
ELT	34.95	29.67	106.57	22.73
ESK	356.8	55.32	77.09	52.75
EWA	202	21.32	-90.01	21.37
EYR	172.4	-43.4	-103.47	-50.06
FCC	265.91	58.76	-27.24	68.75
FHB	310.32	62	38.89	67.62
FIT	279.05	28.07	-7.69	39.31
FMC	248.79	56.66	-51.71	64.36
FRD	282.63	38.2	-1.83	48.85
FRN	240.28	37.09	-56.15	42.98
FSP	238.77	61.76	-66.72	67.38
FUR	11.28	48.17	86.74	43.52
FYU	214.78	66.56	-94.43	67.33
GAK	214.87	62.39	-91.43	63.14
GDH	306.47	69.25	39.4	75.45
GIM	265.36	56.38	-27.68	66.44
GLN	262.88	49.65	-30.45	59.66
GUA	144.87	13.59	-144.04	6.17
GUI	343.57	28.32	60.53	16.49

IAGA	GEOLON	GEOLAT	MAGLON	MAGLAT
GZH	113.34	23.09	-174.75	16.44
HAD	355.52	50.98	74.53	47.66
HAN	26.6	62.25	104.39	58.68
HBK	27.71	-25.88	95.28	-35.96
HER	19.23	-34.43	82.83	-42.28
HLP	18.82	54.61	95	50.77
HOB	147.35	-42.88	-133.2	-53.89
HON	202	21.32	-90.01	21.37
HOR	15.6	77	108.98	74.17
HRB	18.19	47.86	92.68	43.15
HRN	15.6	77	108.98	74.17
HTY	139.8	33.12	-148.49	26.17
HUA	284.67	-12.05	-3.57	0.4
IQA	291.48	63.75	14.85	72.54
IRT	104.45	52.17	177.49	47.48
ISK	29.06	41.07	101.53	35.59
ISL	265.34	53.86	-27.34	64.02
IVA	27.29	68.56	108.38	65.14
JAN	351.3	70.9	82.94	70.24
KAG	130.72	31.48	-157.16	24.8
KAK	140.18	36.23	-148.04	29.35
KAT	117.62	-33.68	-171.03	-46.09
KAV	216.35	70.14	-96.53	71.15
KDU	132.47	-12.69	-155.21	-21.81
KEV	27.01	69.76	109.02	66.37
KIL	20.77	69.06	103.59	65.94
KIR	20.42	67.84	102.43	64.7
KNY	130.88	31.42	-157	24.73
KOU	307.27	5.21	23.53	9.45
KTN	137.71	75.94	-158.19	70.4
KUV	302.82	74.57	42.42	80.91
LEM	147.5	-42.3	-133.21	-53.23
LER	358.82	60.13	80.82	57.99
LMM	32.58	-25.92	100.12	-35.87
LOV	17.83	59.35	95.85	55.92
LRM	115	-21	-173.24	-31.73
LRV	338.3	64.18	66.75	64.91
LVV	23.75	49.9	98.08	45.51
LYR	15.83	78.2	111.39	75.3
LZH	103.85	36.09	176.31	30.58
MAB	5.68	50.3	82.6	46.23

IAGA	GEOLON	GEOLAT	MAGLON	MAGLAT
MAS	23.7	69.46	106.18	66.21
MAW	62.88	-67.61	90.27	-70.25
MBO	343.03	14.38	57.82	1.31
MCM	166.67	-77.85	-32.9	-79.92
MCQ	158.95	-54.5	-111.74	-64.39
MEA	246.65	54.62	-53.74	61.94
MGD	150.86	59.97	-140.35	53.9
MLT	30.89	29.52	102.5	21.93
MMB	144.19	43.91	-144.33	37.13
MSR	142.27	44.37	-146.03	37.66
MUO	23.53	68.02	105.01	64.74
MUT	121.02	14.37	-167.38	7.21
NAL	11.95	78.92	110.45	76.24
NAQ	314.56	61.16	43.08	65.93
NCK	16.72	47.63	91.33	42.87
NEW	242.88	48.27	-56.3	54.81
NGK	12.68	52.07	89	48.08
NOK	88.1	69.4	161.98	64.86
NRD	343.33	81.6	103.17	81.08
NUR	24.65	60.5	102.03	56.91
NVS	82.9	55.03	155.72	50.86
ONW	141.47	38.43	-146.8	31.57
OSO	286.91	-40.34	-0.49	-26.59
OTT	284.45	45.4	1.43	55.66
OUJ	27.23	64.52	105.97	61.01
PAC	289.91	-40.34	1.52	-26.69
PAF	70.26	-49.35	122.32	-58.57
PBK	170.9	70.08	-129.92	65.4
PBQ	282.26	55.28	-0.94	65.47
PEL	24.08	66.9	104.72	63.57
PET	158.25	52.97	-133.12	46.49
PHU	105.95	21.03	177.86	14.17
PIN	263.96	50.2	-28.94	60.33
PKR	212.57	65.12	-95.22	65.48
PNT	289.1	-53.2	2.75	-38.7
PPI	131.73	42.98	-155.7	36.69
PPT	210.42	-17.57	-74.62	-16.66
PST	302.11	-51.7	10.5	-38.31
PUT	290.5	-18.33	1.56	-5.93
QSB	35.64	33.87	107.42	27.75
RAL	256.32	58.22	-41.82	67.14

IAGA	GEOLON	GEOLAT	MAGLON	MAGLAT
RAN	267.89	62.82	-24.87	72.67
RES	265.11	74.69	-39.08	83.08
RIK	143.76	43.48	-144.7	36.7
RVK	10.99	64.94	93.11	62.22
SBA	166.78	-77.85	-32.9	-79.9
SCO	338.03	70.48	72.06	71.51
SER	288.87	-30	0.13	-16.93
SIT	224.67	57.06	-79.4	59.76
SJG	293.85	18.11	10.68	27.69
SKT	307.1	65.42	37.09	71.64
SMI	248.07	60.03	-54.08	67.51
SOD	26.63	67.37	107.07	63.95
SOR	22.22	70.54	105.9	67.37
SPA	0	-90	18.94	-74.1
SPT	355.65	39.55	71.88	32.06
STF	309.28	67.02	40.84	72.82
STJ	307.32	47.6	31.19	53.22
SUA	26.25	45.32	99.48	40.38
SVS	294.9	76.02	33.27	83.29
TAL	266.45	69.54	-30.27	78.68
TAM	5.53	22.79	78.33	9.43
TAN	47.55	-18.92	116.86	-28.71
TAR	26.46	58.26	102.76	54.51
TEO	260.82	19.75	-30.48	29
THL	290.77	77.47	29.74	85.03
THY	17.54	46.9	91.89	42.02
TIK	128.92	71.59	-162.33	66.14
TND	124.95	1.29	-163.48	-6.59
TRO	18.94	69.66	102.64	66.65
TRW	294.68	-43.25	4.91	-29.77
TSU	17.7	-19.22	86.99	-30.48
TUC	249.27	32.17	-45.16	39.76
UMQ	307.87	70.68	42.73	76.57
UPN	303.85	72.78	40.45	79.15
UPS	17.35	59.9	95.68	56.53
VAL	349.75	51.93	70.23	49.39
VIC	236.58	48.52	-63.52	53.73
VLD	286.86	-39.48	-0.62	-25.78
VRE	292.38	-17.28	3.29	-5.19
VSS	316.35	-22.4	23.13	-17.96
WEP	141.88	-12.68	-145.27	-21.42

IAGA	GEOLON	GEOLAT	MAGLON	MAGLAT
WEP	141.88	-12.68	-145.27	-21.42
WEW	143.62	-3.55	-144.3	-11.56
WNG	9.07	53.75	86.5	50.13
YKC	245.52	62.48	-58.77	69.39

References

Akasofu, S.-I. (2007). *Exploring the secrets of the aurora.* Springer Netherlands. Retrieved from https://link.springer.com/book/10.1007/0-306-47970-2

Baker, D., Balstad, R., Bodeau, M., Cameron, E., Fennell, J., Forbes, K., ... Strachan, L. (2008). *Severe space weather events: Understanding societal and economic impacts: A workshop report.* Washington, DC: The National Academies Press. Retrieved from https://nap.nationalacademies.org/catalog/12507/severe-space-weather-events-understanding-societal-and-economic-impacts-a doi: 10.17226/12507

Barbosa, C. S., Alves, L. R., Caraballo, R., Hartmann, G. A., Papa, A. R. R., & Pirjola, R. J. (2015). Analysis of geomagnetically induced currents at a low-latitude region over the solar cycles 23 and 24: comparison between measurements and calculations. *Journal of Space Weather and Space Climate*, *5*.

Batista, I. S., Abdu, M. A., de Souza, J. R., Bertoni, F. C. P., Matsuoka, M. T., de Oliveira Camargo, P., & Bailey, G. J. (2006). Unusual early morning development of the equatorial anomaly in the brazilian sector during the halloween magnetic storm. *Journal of Geophysical Research*, *111*, 10.

Belakhovsky, V. B., Pilipenko, V. A., Engebretson, M. J., Sakharov, Y., & Selivanov, V. (2019). Impulsive disturbances of the geomagnetic field as a cause of induced currents of electric power lines. *Journal of Space Weather and Space Climate*.

Belakhovsky, V. B., Pilipenko, V. A., Sakharov, Y. A., & Selivanov, V. (2018). Characteristics of the variability of a geomagnetic field for studying the impact of the magnetic storms and substorms on electrical energy systems. *Izvestiya, Physics of the Solid Earth*, *54*, 52-65.

Berger, T. E., Holzinger, M. J., Sutton, E. K., & Thayer, J. P. (2020). Flying through uncertainty. *Space Weather*, *18*(1), e2019SW002373. Retrieved from https://agupubs.onlinelibrary.wiley.com/doi/abs/10.1029/2019SW002373 (e2019SW002373 2019SW002373) doi: https://doi.org/10.1029/2019SW002373

Boteler, Pirjola, R., & Nevanlinna, H. (1998). The effects of geomagnetic disturbances on electrical systems at the earth's surface. *Advances in Space Research*, *22*(1), 17-27. Retrieved from https://www.sciencedirect.com/science/article/pii/S027311779701096X (Solar-Terrestrial Relations: Predicting the Effects on the Near-Earth Environment) doi: https://doi.org/10.1016/S0273-1177(97)01096-X

Boteler, D. H. (2019). A 21st century view of the march 1989 magnetic storm. *Space Weather*, *17*(10), 1427-1441. Retrieved from https://agupubs.onlinelibrary.wiley.com/doi/abs/10.1029/2019SW002278 doi: https://doi.org/10.1029/2019SW002278

Buck, J. R., Daniel, M. M., & Singer, A. C. (2002). *Computer explorations in signals and systems using matlab, 2e.* Retrieved from https://www.mathworks.com/academia/books/computer-explorations-in-signals-and-systems-using-matlab-buck.html

Clark, A. (2015). *Pillow (pil fork) documentation.* readthedocs. Retrieved from https://buildmedia.readthedocs.org/media/pdf/pillow/latest/pillow.pdf

Dimmock, A. P., Rosenqvist, L., Hall, J.-O., Viljanen, A., Yordanova, E., Honkonen, I., ... Sjöberg, E. C. (2019). The gic and geomagnetic response over fennoscandia to the 7–8 september 2017 geomagnetic storm. *Space Weather*, *17*, 1010 - 989.

Eastwood, J. P., Biffis, E., Hapgood, M. A., Green, L., Bisi, M. M., Bentley, R. D., ... Burnett, C. (2017). The economic impact of space weather: Where do we stand? *Risk Analysis*, *37*(2), 206-218. Retrieved from https://onlinelibrary.wiley.com/doi/abs/10.1111/risa.12765 doi: https://doi.org/10.1111/risa.12765

Ebihara, Y., ichi Watari, S., & Kumar, S. (2021). Prediction of geomagnetically induced currents (GICs) flowing in japanese power grid for carrington-class magnetic storms. *Earth, Planets and Space*, *73*, 1-10.

Engebretson, M. J., Pilipenko, V. A., Ahmed, L. Y., Posch, J. L., Steinmetz, E. S., Moldwin, M. B., ... Vorobev, A. V. (2019). Nighttime magnetic perturbation events observed in arctic canada: 1. survey and statistical analysis. *Journal of Geophysical Research: Space Physics*, *124*, 7442 - 7458.

Engebretson, M. J., Pilipenko, V. A., Steinmetz, E. S., Moldwin, M. B., Connors, M. G., Boteler, D. H., ... Russell, C. T. (2020). Nighttime magnetic perturbation events observed in arctic canada: 3. occurrence and amplitude as functions of magnetic latitude, local time, and magnetic disturbance indices. *Space Weather*, *19*.

FEMA Homeland Security. (2019, May). Federal Operating Concept for Impending Space Weather Events.

Forbes, T. G. (2000). A review on the genesis of coronal mass ejections. *Journal of Geophysical Research: Space Physics*, *105*(A10), 23153-23166. doi: 10.1029/2000JA000005

Gannon, J. (2019). *Geomagnetically induced currents from the sun to the power grid* (J. L. Gannon, A. Swidinsky, & Z. Xu, Eds.). Nashville, TN: John Wiley & Sons.

Gjerloev, J. W. (2012). The supermag data processing technique. *Journal of Geophysical Research: Space Physics*, *117*(A9). Retrieved from https://agupubs.onlinelibrary.wiley.com/doi/abs/10.1029/2012JA017683 doi: https://doi.org/10.1029/2012JA017683

Harris, C. R., Millman, K. J., van der Walt, S. J., Gommers, R., Virtanen, P., Cournapeau, D., ... Oliphant, T. E. (2020, September). Array programming with NumPy. *Nature*, *585*(7825), 357–362. Retrieved from https://doi.org/10.1038/s41586-020-2649-2 doi: 10.1038/s41586-020-2649-2

Hathaway, D. H., & Wilson, R. M. (2006). Geomagnetic activity indicates large amplitude for sunspot cycle 24. *Geophysical Research Letters*, *33*.

Hood, A. W., & Priest, E. R. (1979, December). Kink instability of solar coronal loops as the cause of solar flares. *Solar Physics*, *64*(2), 303–321. Retrieved from https://doi.org/10.1007/BF00151441 doi: 10.1007/BF00151441

Hu, H. (2023, April). *Investigating the Space Weather Impact of the 2003 Halloween Geomagnetic Storm by the Ground Magnetic Field Variations: a Global View.* Zenodo. Retrieved from https://doi.org/10.5281/zenodo.7830370 (If you use this software, please cite it as below.) doi: 10.5281/zenodo.7830370

Hunter, J. D. (2007). Matplotlib: A 2d graphics environment. *Computing in Science & Engineering*, *9*(3), 90–95. doi: 10.1109/MCSE.2007.55

Inc., T. M. (2022). *Matlab version: 9.13.0 (r2022b).* Natick, Massachusetts, United States: Author Retrieved from https://www.mathworks.com

Kamide, Y. (2006). What is an "intense geomagnetic storm"? *Space Weather*, *4*(6). Retrieved from https://agupubs.onlinelibrary.wiley.com/doi/abs/10.1029/2006SW000248 doi: https://doi.org/10.1029/2006SW000248

Knipp, D. J. (2015). Synthesis of geomagnetically induced currents: Commentary and research. *Space Weather*, *13*(11), 727-729. Retrieved from https://agupubs.onlinelibrary.wiley.com/doi/abs/10.1002/2015SW001317 doi: https://doi.org/10.1002/2015SW001317

Kotzé, P. B., Cilliers, P. J., & Sutcliffe, P. R. (2015). The role of sansa's geomagnetic observation network in space weather monitoring: A review. *Space Weather*, *13*(10), 656-664. Retrieved from https://agupubs.onlinelibrary.wiley.com/doi/abs/10

.1002/2015SW001279 doi: https://doi.org/10.1002/2015SW001279

Kusano, K., Bamba, Y., Yamamoto, T. T., Iida, Y., Toriumi, S., & Asai, A. (2012, oct). MAGNETIC FIELD STRUCTURES TRIGGERING SOLAR FLARES AND CORONAL MASS EJECTIONS. *The Astrophysical Journal*, *760*(1), 31. Retrieved from https://doi.org/10.1088%2F0004-637x%2F760%2F1%2F31 doi: 10.1088/0004-637x/760/1/31

Kusano, K., Maeshiro, T., Yokoyama, T., & Sakurai, T. (2004). The trigger mechanism of solar flares in a coronal arcade with reversed magnetic shear. *The Astrophysical Journal*, *610*, 537 - 549.

Love, J. J., Lucas, G. M., Kelbert, A., & Bedrosian, P. A. (2018). Geoelectric hazard maps for the mid-atlantic united states: 100 year extreme values and the 1989 magnetic storm. *Geophysical Research Letters*, *45*(1), 5-14. Retrieved from https://agupubs.onlinelibrary.wiley.com/doi/abs/10.1002/2017GL076042 doi: https://doi.org/10.1002/2017GL076042

Marshall, R. A., Dalzell, M., Waters, C. L., Goldthorpe, P., & Smith, E. A. (2012). Geomagnetically induced currents in the new zealand power network. *Space Weather*, *10*(8). Retrieved from https://agupubs.onlinelibrary.wiley.com/doi/abs/10.1029/2012SW000806 doi: https://doi.org/10.1029/2012SW000806

Maus, S., & Lühr, H. (2005). Signature of the quiet-time magnetospheric magnetic field and its electromagnetic induction in the rotating earth. *Geophysical Journal International*, *162*(3), 755-763. Retrieved from https://onlinelibrary.wiley.com/doi/abs/10.1111/j.1365-246X.2005.02691.x doi: https://doi.org/10.1111/j.1365-246X.2005.02691.x

Mcallister, A. H., Dryer, M., Mclntosh, P. S., Singer, H. J., & Weiss, L. A. (1996). A large polar crown coronal mass ejection and a “problem” goemagnetic storm: April 14–23, 1994. *Journal of Geophysical Research: Space Physics*, *101*, 13497 - 13515.

National Space Weather Strategy and Action Plan. (2019, March). Retrieved from https://trumpwhitehouse.archives.gov/wp-content/uploads/2019/03/National-Space-Weather-Strategy-and-Action-Plan-2019.pdf

Ngwira, C. M., Pulkkinen, A., Bernabeu, E., Eichner, J. F., Viljanen, A., & Crowley, G. (2015). Characteristics of extreme geoelectric fields and their possible causes: Localized peak enhancements. *Geophysical Research Letters*, *42*, 6916 - 6921.

Ngwira, C. M., Pulkkinen, A., Wilder, F. D., & Crowley, G. (2013). Extended study of extreme geoelectric field event scenarios for geomagnetically induced current applications. *Space Weather*, *11*, 121 - 131.

Orr, L., Chapman, S. C., & Beggan, C. D. (2021). Wavelet and network analysis of magnetic field variation and geomagnetically induced currents during large storms. *Space Weather*, *19*(9), e2021SW002772. Retrieved from https://agupubs.onlinelibrary.wiley.com/doi/abs/10.1029/2021SW002772 (e2021SW002772 2021SW002772) doi: https://doi.org/10.1029/2021SW002772

Osella, A., Favetto, A., & López, E. (1998). Currents induced by geomagnetic storms on buried pipelines as a cause of corrosion. *Journal of Applied Geophysics*, *38*(3), 219-233. Retrieved from https://www.sciencedirect.com/science/article/pii/S0926985197000190 doi: https://doi.org/10.1016/S0926-9851(97)00019-0

pandas development team, T. (2020, February). *pandas-dev/pandas: Pandas.* Zenodo. Retrieved from https://doi.org/10.5281/zenodo.3509134 doi: 10.5281/zenodo.3509134

Pulkkinen, A., Bernabeu, E., Thomson, A., Viljanen, A., Pirjola, R., Boteler, D., … MacAlester, M. (2017). Geomagnetically induced currents: Science, engineering, and applications readiness. *Space Weather*, *15*(7), 828-856. Retrieved from https://agupubs.onlinelibrary.wiley.com/doi/abs/10.1002/2016SW001501 doi: https://doi.org/10.1002/2016SW001501

S, I., A, M., H, T., & T, I. (2022). *Mid-latitude geomagnetic indices asy and sym (asy/sym indices)* [database]. World Data Center for Geomagnetism, Kyoto. Retrieved from https://wdc.kugi.kyoto-u.ac.jp/aeasy/index.html doi: 10.14989/267216

Schultz, C. (2012). Solar storms can destabilize power grids at midlatitudes. *Eos, Transactions American Geophysical Union*, *93*(41), 412-412. Retrieved from https://agupubs.onlinelibrary.wiley.com/doi/abs/10.1029/2012EO410020 doi: https://doi.org/10.1029/2012EO410020

Shibata, K., & Magara, T. (2011). Solar flares: Magnetohydrodynamic processes. *Living Reviews in Solar Physics*, *8*, 1-99.

Shiokawa, K. (2023). Introduction of space weather research on magnetosphere and ionosphere of the earth. In K. Kusano (Ed.), *Solar-terrestrial environmental prediction* (pp. 95–113). Singapore: Springer Nature Singapore. Retrieved from https://doi.org/10.1007/978-981-19-7765-7_4 doi: 10.1007/978-981-19-7765-7_4

Simpson, F., & Bahr, K. (2020). Estimating the electric field response to the halloween 2003 and september 2017 magnetic storms across scotland using observed geomagnetic fields, magnetotelluric impedances and perturbation tensors. *Journal of Space Weather and Space Climate*, *10*(1), 48-. Retrieved from http://www.sciengine.com/publisher/EDPSciences/journal/JournalofSpaceWeatherandSpaceClimate/10/1/10.1051/swsc/2020049 doi: https://doi.org/10.1051/swsc/2020049

Srivastava, N., & Venkatakrishnan, P. (2002). Relationship between cme speed and geomagnetic storm intensity. *Geophysical Research Letters*, *29*(9), 1-1-1-4. Retrieved from https://agupubs.onlinelibrary.wiley.com/doi/abs/10.1029/2001GL013597 doi: https://doi.org/10.1029/2001GL013597

Stoica, P., & Moses, R. L. (2005). *Spectral analysis of signals*. Pearson/Prentice Hall.

SuperMAG. (2009). [database]. Retrieved from https://supermag.jhuapl.edu/mag/?fidelity=low&start=2003-10-29T00\%3A00\%3A00.000Z&interval=23\%3A59&tab=customdownload&stations=YKC,CBB,RES,BLC,MEA,SIT,PBQ,STJ,ALE,LRV,BOU,FRN,VIC,NEW,LOV,LER,VAL,HAD,ESK,MAB,DOU,BFE,CLF,OTT,WNG,VRE,THY,BEL,FUR,NGK,BDV,FRD,THL,SVS,KUV,UPN,UMQ,GDH,ATU,STF,SKT,FHB,NAQ,NRD,DMH,DNB,SCO,AMK,GIM,TAL,CNL,DAW,FCC,FMC,FSP,SMI,ISL,PIN,RAL,RAN,NAL,LYR,JAN,BJN,SOR,TRO,AND,RVK,DOB,HRN,KEV,MAS,KIL,IVA,ABK,MUO,KIR,SOD,PEL,OUJ,HAN,NUR,UPS,TAR,BRW,KAV,ARC,BET,FYU,EAG,CMO,GAK,PKR,CCS,TIK,AAE,ABG,AMS,API,ASP,BMT,BNG,BSL,CNB,CAN,CZT,DLR,DRV,EYR,GUA,GUI,HBK,HER,HLP,HON,HRB,IQA,IRT,ISK,KAK,KOU,MBO,MMB,NCK,PAF,PHU,PPT,SBA,SJG,SPT,SUA,TAM,TAN,TUC,VSS,NVS,LVV,PPI,MUT,LRM,KAT,KTN,CHD,MGD,MSR,ONW,KAG,CBI,WEW,WEP,EWA,MCQ,PBK,AIA,ASC,CSY,CTA,GLN,HTY,KDU,KNY,MAW,PST,TSU,HUA,TRW,AQU,LMM,LZH,QSB,TND,EBR,TEO,LEM,RIK,FIT,PUT,SER,CER,VLD,OSO,PNT,PAC,MCM,SPA,ELT,GZH,MLT,NOK,B11,B12,B14,B15,B17,B18,B19,B20,B21,B22,B23,B03,B04,HOR,PET,CUL,HOB

The Solar and Heliospheric Observatory (SOHO) Project Scientist Team. (2018). [database]. Retrieved from https://sohoftp.nascom.nasa.gov/sdb/goes/ace/daily/20031029_ace_mag_1m.txt

Torta, J. M., Marsal, S., & Quintana, M. (2014). Assessing the hazard from geomagnetically induced currents to the entire high-voltage power network in spain. *Earth, Planets and Space*, *66*, 1-17.

Tóth, G., De Zeeuw, D. L., Gombosi, T. I., Manchester, W. B., Ridley, A. J., Sokolov, I. V., & Roussev, I. I. (2007). Sun-to-thermosphere simulation of the 28–30 october 2003 storm with the space weather modeling framework. *Space Weather*, *5*(6). Retrieved from https://agupubs.onlinelibrary.wiley.com/doi/abs/10.1029/2006SW000272 doi: https://doi.org/10.1029/2006SW000272

Viljanen, A. (1997). The relation between geomagnetic variations and their time derivatives and implications for estimation of induction risks. *Geophysical Research Letters*, *24*(6), 631-634. Retrieved from https://agupubs.onlinelibrary.wiley.com/doi/abs/10.1029/97GL00538 doi: https://doi.org/10.1029/97GL00538

Villante, U., & Regi, M. (2008). Solar flare effect preceding halloween storm (28 october 2003): Results of a worldwide analysis. *Journal of Geophysical Research: Space Physics*, *113*(A3). Retrieved from https://agupubs.onlinelibrary.wiley.com/

doi/abs/10.1029/2008JA013132 doi: https://doi.org/10.1029/2008JA013132

Waskom, M. L. (2021). seaborn: statistical data visualization. *Journal of Open Source Software*, *6*(60), 3021. Retrieved from https://doi.org/10.21105/joss.03021 doi: 10.21105/joss.03021

Webb, D. F., Cliver, E. W., Crooker, N. U., Cyr, O. C. S., & Thompson, B. J. (2000). Relationship of halo coronal mass ejections, magnetic clouds, and magnetic storms. *Journal of Geophysical Research*, *105*, 7491-7508.

Wes McKinney. (2010). Data Structures for Statistical Computing in Python. In Stéfan van der Walt & Jarrod Millman (Eds.), *Proceedings of the 9th Python in Science Conference* (p. 56 - 61). doi: 10.25080/Majora-92bf1922-00a

Woodroffe, J. R., Morley, S. K., Jordanova, V. K., Henderson, M. G., Cowee, M. M., & Gjerloev, J. G. (2016). The latitudinal variation of geoelectromagnetic disturbances during large (dst $<$ -100 nt) geomagnetic storms. *Space Weather*, *14*(9), 668-681. Retrieved from https://agupubs.onlinelibrary.wiley.com/doi/abs/10.1002/2016SW001376 doi: https://doi.org/10.1002/2016SW001376

World Data Center for Geomagnetism, Kyoto. (2018). [database]. Retrieved from https://wdc.kugi.kyoto-u.ac.jp/aeasy/index.html

Xu, Z., Gannon, J. L., & Rigler, E. J. (2013). Report of geomagnetic pulsation indices for space weather applications..